or retrograde labeling) with retinal thickness (e.g., RNFL or GCC thicknesses) in the same eyes, the studies[4,10] suggest that retinal thinning is likely the event that results from optic nerve crush-induced RGC injury. Consistently, the reduction of RGCs seen as Thy 1-CFP expression in our study, apparently occurred several days before the thinning of the inner retinal layers, particularly RNFL; however, there are several concerns regarding the interpretation of the results.

One concern regarding the temporally different patterns of reduction in the number of CFP-positive RGCs and GCC thickness is the initial inflammatory response, which can mask the thinning of the nerve fiber layers. The swelling of IPL seen in the histologic sections on day 1 suggested the existence of an inflammatory response, which may increase GCC thickness. Mild GCC thickening was also seen from 1 to 4 days after injection in the PBS-injected control eyes (Fig. 5). Therefore, the thickening may be caused by the inflammatory reaction induced by the intravitreal injection itself rather than by the NMDA injection.

Another concern regarding the temporally different patterns of reduction in the above-mentioned two parameters is the possibility of CFP downregulation that occurs before RGC death. Schlamp et al.[31] demonstrated that by 6 hours after NMDA injection, the *Thy1* mRNA levels in the RGC starts to decrease, whereas there is no apparent change in the number of the cells present in the GCL. By 48 hours, the expression level of *Thy1* mRNA or Thy1-expressing cells decreases to less than 20% of the control fellow eyes, whereas more than half of the cells remained in the GCL. Similar earlier loss of Thy 1 expression in RGCs preceding the loss of RGC numbers on histologic or imaging studies has been documented in an optic nerve crush model.[7] The early loss of Thy 1 expression is consistent with the report that the damaged RGCs undergo a shutdown of many normally expressed genes as an early step in apoptosis.[32] In our immunohistochemical analysis, 1 day after NMDA injection, GFP-positive RGCs decreased to 34.6% of the preinjection level, which was comparable to 27.1% observed on the scSLO images. On the other hand, GFP-negative RGCs increased to more than two times the preinjection level, suggesting that CFP downregulation actually occurred in some cells. However, RGCs (all the HPC-1-negative cells in GCL) indeed decreased to 65.2% of the preinjection level. Moreover, the cells in GCL, counted on the HE-stained sections on day 1, were 72.6% of the preinjection level. Therefore, although downregulation of CFP expression occurred before the disappearance of the somas of some RGCs, these observations indicate that thinning of the inner retinal layers is an event resulting from the loss of RGCs in NMDA-induced retinal injuries.

CFP expression in Thy 1-CFP mouse line has been reported to localize not only to RGCs but also to a subpopulation of displaced amacrine cells.[30] It has been reported that the displaced amacrines are small and emit weakly fluorescent signals. Therefore, we believe that weakly fluorescent small cells in the scSLO images in this study are mainly displaced amacrines. Indeed, the weakly fluorescent small cells accounted for 10.5% of all the CFP-positive cells, a finding consistent with a study by Raymond et al.,[30] in which 9.6% of the CFP-positive cells were HPC-1-positive amacrines. On the basis of this evidence, we believe that the CFP-positive cells, other than the weakly fluorescent small cells, are mainly RGCs, and used the number of CFP-expressing cells, excluding the weakly fluorescent small cells, as the number of CFP-expressing RGCs. Our immunohistochemical analysis showed that 14 days after NMDA injection, GFP-positive displaced amacrine cells (HPC-1-positive) decreased to only 78.5% of that on day 0, indicating that they are resistant to NMDA insult. Furthermore, the HPC-1-positive cells were 34.6% of the remaining GFP-positive cells on day 14; this was comparable to the result of scSLO that weakly fluorescent small cells were 46.7% of all the CFP-positive cells. Consideration of all the points, however, indicates that many of the remaining cells after NMDA insult were surviving RGCs. Thus, the RGCs that were resistant to one-time NMDA injection might account for the plateau that was seen in the time course of changes in the number of CFP-positive cells on the scSLO images in this study, although the appearance of the plateau may be partly explained by the existence of the less vulnerable displaced amacrine cells.

We also evaluated the potential difference in the vulnerability to NMDA insult among the different sizes of the RGCs using the scSLO images. Fourteen days after NMDA injection, the number of CFP-expressing large RGCs decreased to 18.8% of the preinjection level, whereas the number of CFP-expressing small RGCs decreased to 23.3% of the preinjection level. Therefore, on the basis of the size of the RGCs using scSLO images, the vulnerability to NMDA did not significantly differ between the cell types.

In clinical studies, circumpapillary retinal nerve fiber layer (cpRNFL) thickness is widely used to discriminate eyes with glaucoma. In human and mouse eyes, assessment of the RNFL thickness on a circular scan around the optic nerve head appears ideal for evaluating RGC damage because it is capable of detecting all RGC axons that converge toward the optic nerve head in both species. However, RNFLs in mice are much thinner than those of humans and are much more difficult to measure, particularly in damaged retinas. In this study, besides GCC thinning in the damaged retinas, the layer boundaries also became unclear, probably because the loss of the somas, axons, and dendrites of RGCs and changes in glial components decreased the reflectivity of the diminished RNFL, GCL, and IPL. The GCC is an alternative to the RNFL for assessing RGC damage, since the GCC includes RGC axons as RNFL and RGC somas as GCL. GCC is thicker than RNFL only, allowing easier delineation in all eyes. In patients with glaucoma, GCC thickness in the macula has been shown to have glaucoma discriminating ability that is comparable to cpRNFL thickness.[15–18] However, mouse eyes do not have a macula. Therefore, instead of measuring macular GCC thickness or cpRNFL thickness, we thought it practically appropriate to use GCC thickness around the optic nerve head to detect glaucomatous damage. Because it is uncertain which scan pattern for sampling is appropriate for GCC measurements in mice, we compared the most standard scan patterns around the optic nerve head; the circular scan versus radial scans. We found a strong correlation between these scan patterns. In addition, we were able to detect a characteristic slow decrease in GCC thickness on a circular scan in the mouse eyes injected with NMDA consistent with the results of previous studies.[10] We also confirmed the reliability of the manual measurement of GCC thickness. These observations show that GCC thickness on a circular scan around the optic disc is an ideal and useful parameter for evaluating RGC damage in mice.

Then, we examined NMDA dose-dependent changes in the number of RGCs and GCC thickness and elucidated that more than 10 nanomoles of NMDA is necessary to induce severe reduction in of the number of RGCs and GCC thickness. Eyes injected with 2 nanomoles of NMDA showed milder and slower damage both to RGCs and GCCs compared with higher concentrations of NMDA. However, in eyes injected with 5 nanomoles of NMDA, although the loss of RGCs was comparable to that in eyes injected with 2 nanomoles NMDA, GCC thinning was as severe as in eyes injected with 10 nanomoles or more of NMDA. The difference in the effect of damage on the number of RGCs and in GCC thickness in eyes injected with 5 nanomoles of NMDA may be attributable to the fact that GCC includes RNFL and IPL in addition to GCL. Some cells in the INL other than RGCs are known to be damaged by NMDA. Because the IPL consists of the nerve fibers from cells in the INL, damage to cells in the INL leads to IPL thinning. The sensitivity to NMDA may differ between RGCs and cells in the INL. This possibility remains to be clarified.

Application of retinal imaging technologies to mice, particularly those with genetic cellular markers, allows noninvasive longitudinal assessment of neuronal damage such as loss of cell bodies and tissue atrophy. Experimental mouse models are most widely used to investigate the pathophysiology of human diseases; various transgenic and knockout mice as well as natural mutants are available for use in the investigation of the role of a molecule in vivo. The noninvasive nature of this approach does not require animals to be euthanized and enables us to examine exactly the same region in the same eye via in vivo sequential imaging, allowing for use of a minimal number of animals. Compared with histologic methods, our double-imaging approach in particular has a great advantage in monitoring both the individual RGC loss and the RGC-related layer thinning on sectional images in the same diseased eyes. Our findings with regard to the different time courses of the two RGC-related parameters were strengthened by measuring both parameters simultaneously in the identical eyes. Thus, the simultaneous imaging of two parameters in the mouse fundus, as shown in this study, would potentially be widely used as a useful tool for basic and translational research of the examination of pathologic mechanisms of RGC damage, as well as for investigation of new treatments for glaucoma.

In summary, we were able to show time-dependent changes in Thy 1-CFP-expressing RGCs and GCC thickness in the identical eyes with an NMDA-induced RGC injury by using a combined system of scSLO and speckle noise–reduced SD-OCT. We found that the reduction in these two parameters show different time courses. Co-monitoring of CFP-expressing RGCs and GCC thickness in mice would contribute to investigation of the longitudinal profile of RGC degeneration.

Acknowledgments

The authors thank Yuri Terado, Noriko Suzuki, Michiko Tsuji, and Keiko Kuroiwa for their technical assistance, Akiko Hirata for her contribution to the reliability assessment of the manual measurement of GCC thickness on SD-OCT images, and Gerhard Zinser for useful discussions of the Multiline instrument.

References

1. Quigley HA. Number of people with glaucoma worldwide. *Br J Ophthalmol.* 1996;80:389-393.
2. Fechtner RD, Weinreb RN. Mechanisms of optic nerve damage in primary open angle glaucoma. *Surv Ophthalmol.* 1994;39:23-42.
3. Cordeiro MF, Guo L, Luong V, et al. Real-time imaging of single nerve cell apoptosis in retinal neurodegeneration. *Proc Natl Acad Sci U S A.* 2004;101:13352-13356.
4. Higashide T, Kawaguchi I, Ohkubo S, Takeda H, Sugiyama K. In vivo imaging and counting of rat retinal ganglion cells using a scanning laser ophthalmoscope. *Invest Ophthalmol Vis Sci.* 2006; 47:2943-2950.
5. Srinivasan VJ, Ko TH, Wojtkowski M, et al. Noninvasive volumetric imaging and morphometry of the rodent retina with high-speed, ultrahigh-resolution optical coherence tomography. *Invest Ophthalmol Vis Sci.* 2006;47:5522-5528.
6. Leung CK, Lindsey JD, Crowston JG, et al. In vivo imaging of murine retinal ganglion cells. *J Neurosci Methods.* 2008;168:475-478.
7. Leung CK, Lindsey JD, Crowston JG, Lijia C, Chiang S, Weinreb RN. Longitudinal profile of retinal ganglion cell damage after optic nerve crush with blue-light confocal scanning laser ophthalmoscopy. *Invest Ophthalmol Vis Sci.* 2008;49:4898-4902.
8. Murata H, Aihara M, Chen YN, Ota T, Numaga J, Araie M. Imaging mouse retinal ganglion cells and their loss in vivo by a fundus camera in the normal and ischemia-reperfusion model. *Invest Ophthalmol Vis Sci.* 2008;49:5546-5552.
9. Leung CK, Lindsey JD, Chen L, Liu Q, Weinreb RN. Longitudinal profile of retinal ganglion cell damage assessed with blue-light confocal scanning laser ophthalmoscopy after ischaemic reperfusion injury. *Br J Ophthalmol.* 2009;93:964-968.
10. Nagata A, Higashide T, Ohkubo S, Takeda H, Sugiyama K. In vivo quantitative evaluation of the rat retinal nerve fiber layer with optical coherence tomography. *Invest Ophthalmol Vis Sci.* 2009; 50:2809-2815.
11. Fischer MD, Huber G, Beck SC, et al. Noninvasive, in vivo assessment of mouse retinal structure using optical coherence tomography. *PLoS One.* 2009;4:e7507.
12. Guo L, Normando EM, Nizari S, Lara D, Cordeiro MF. Tracking longitudinal retinal changes in experimental ocular hypertension using the cSLO and spectral domain-OCT. *Invest Ophthalmol Vis Sci.* 2010;51:6504-6513.
13. Schmitt JM, Xiang SH, Yung KM. Speckle in optical coherence tomography. *J Biomed Opt.* 1999;4:95-105.
14. Hangai M, Yamamoto M, Sakamoto A, Yoshimura N. Ultrahigh-resolution versus speckle noise-reduction in spectral-domain optical coherence tomography. *Opt Express.* 2009;17:4221-4235.
15. Ishikawa H, Stein DM, Wollstein G, Beaton S, Fujimoto JG, Schuman JS. Macular segmentation with optical coherence tomography. *Invest Ophthalmol Vis Sci.* 2005;46:2012-2017.
16. Tan O, Li G, Lu AT, Varma R, Huang D. Advanced imaging for glaucoma study group: mapping of macular substructures with optical coherence tomography for glaucoma diagnosis. *Ophthalmology.* 2008;115:949-956.
17. Tan O, Chopra V, Lu AT, et al. Detection of macular ganglion cell loss in glaucoma by Fourier-domain optical coherence tomography. *Ophthalmology.* 2009;116:2305-2314.
18. Seong M, Sung KR, Choi EH, et al. Macular and peripapillary retinal nerve fiber layer measurements by spectral domain optical coherence tomography in normal-tension glaucoma. *Invest Ophthalmol Vis Sci.* 2010;51:1446-1452.
19. Shaner NC, Steinbach PA, Tsien RY. A guide to choosing fluorescent proteins. *Nat Methods.* 2005;2:905-909.
20. Feng G, Mellor RH, Bernstein M, et al. Imaging neuronal subsets in transgenic mice expressing multiple spectral variants of GFP. *Neuron.* 2000;28:41-51.
21. Morris R. Thy-1 in developing nervous tissue. *Dev Neurosci.* 1985; 7:133-160.
22. Barnstable CJ, Drager UC. Thy-1 antigen: a ganglion cell specific marker in rodent retina. *Neuroscience.* 1984;11:847-855.
23. Siliprandi R, Canella R, Carmignoto G, et al. N-methyl-D-aspartate-induced neurotoxicity in the adult rat retina. *Vis Neurosci.* 1992; 8:567-573.
24. Vorwerk CK, Lipton SA, Zurakowski D, Hyman BT, Sabel BA, Dreyer EB. Chronic low-dose glutamate is toxic to retinal ganglion cells: toxicity blocked by memantine. *Invest Ophthalmol Vis Sci.* 1996;37:1618-1624.
25. Nickells RW. Retinal ganglion cell death in glaucoma: the how, the why, and the maybe. *J Glaucoma.* 1996;5:345-356.
26. Li Y, Schlamp CL, Nickells RW. Experimental induction of retinal ganglion cell death in adult mice. *Invest Ophthalmol Vis Sci.* 1999;40:1004-1008.
27. Ooto S, Hangai M, Sakamoto A, et al. Three-dimensional profile of macular retinal thickness in normal Japanese eyes. *Invest Ophthalmol Vis Sci.* 2010;51:465-473.
28. Soto I, Brian E, Buckingham P, et al. Retinal ganglion cells downregulate gene expression and lose their axons within the optic nerve head in a mouse glaucoma model. *J Neurosci.* 2008;28:548-561.
29. Landis JR, Koch GG. The measurement of observer agreement for categorical data. *Biometrics.* 1977;33:159-174.
30. Raymond ID, Vila A, Huynh UC, Brecha NC. Cyan fluorescent protein expression in ganglion and amacrine cells in a thy1-CFP transgenic mouse retina. *Mol Vis.* 2008;14:1559-1574.
31. Schlamp CL, Johnson EC, Li Y, Morrison JC, Nickells RW. Changes in Thy1 gene expression associated with damaged retinal ganglion cells. *Mol Vis.* 2001;7:192-201.
32. Miller TM, Moulder KL, Knudson CM, et al. Bax deletion further orders the cell death pathway in cerebellar granule cells and suggests a caspase-independent pathway to cell death. *J Cell Biol.* 1997;139:205-217.

Gene Expression Patterns 12 (2012) 36–45

Contents lists available at SciVerse ScienceDirect

Gene Expression Patterns

journal homepage: www.elsevier.com/locate/gep

Spatio-temporal expression pattern of the NatB complex, Nat5/Mdm20 in the developing mouse brain: Implications for co-operative *versus* non-co-operative actions of Mdm20 and Nat5

Kyoji Ohyama [a,*], Kunihiko Yasuda [a], Kazuko Onga [a], Akira Kakizuka [b], Nozomu Mori [a,*]

[a] *Department of Anatomy and Neurobiology, Graduate School of Biomedical Sciences, Nagasaki University, 1-12-4 Sakamoto, Nagasaki 852-8523, Japan*
[b] *Laboratory of Functional Biology, Kyoto University Graduate School of Biostudies, Kyoto 606-8501, Japan*

ARTICLE INFO

Article history:
Received 2 June 2011
Received in revised form 1 November 2011
Accepted 2 November 2011
Available online 10 November 2011

Keywords:
Nat
Mdm20
Acetylation
Post-translation
Mouse
Brain
Neuron

ABSTRACT

The NatB complex, Nat5/Mdm20 acetyltransferase mediates *N*-acetylation to control cell cycle progression and actin dynamics in yeast. As yet, little is known about the expression pattern of Mdm20 and Nat5 in multi-cellular organisms. Here we show that Mdm20 is highly expressed in mouse embryonic brain. At E11.5, Mdm20 was widely expressed in both neural progenitors and early differentiating neurons, whereas Nat5 was expressed in Sox1/3+/Mdm20+ neural progenitors. By E14.5, both Mdm20 and Nat5 were downregulated in most ventricular zone neural progenitors, whereas both proteins were found in differentiating neurons and co-expression was maintained at E18.5 in derivatives of these cells, such as midbrain dopaminergic (DA) neurons and septal neurons. These data suggest that Nat5/Mdm20 complex-mediated acetylation may play a role in the proliferation and differentiation of neural progenitors. Intriguingly, our data also showed that Mdm20 is not always co-expressed with Nat5 in all differentiated neurons, for example deep cerebellar neurons. Moreover, detailed examination of the subcellular localization of Mdm20 and Nat5 in cultured Nat5+/Mdm20+ midbrain DA neurons revealed that Mdm20 is also not necessarily co-localized with Nat5 within neurons. Given that Nat5 is only a known member of Nat family protein that interacts with Mdm20, our data imply that Mdm20 may function either with an unidentified Nat protein partner(s) or possibly in a Nat-independent manner.

Post-translational modification of proteins is critically important in biology and expands both the structural and functional diversity of proteins, contributing to both evolutionary divergence and population diversity (Magalon et al., 2008; Arnesen et al., 2009). Two particular protein modifications, acetylation and phosphorylation, play key roles in a wide range of biological events, including tissue development (Kouzarides, 2000; Choudhary et al., 2009; Sadoul et al., 2010). The sculpting of tissue morphology over time is also dependent on the spatial and temporal control of gene transcription (Dessaud et al., 2007; Ohyama et al., 2008; Pearson et al., 2011), and indeed acetylation and phosphorylation often co-operate to modulate protein activities, which in turn modulate gene transcription (Sims and Reinberg, 2008; Lau and Cheung, 2011). For instance, a lysine acetyltransferase (KAT) – formerly called HAT (histone acetyltransferase) – mediates acetylation of the internal lysine residues of histones which, coupled with histone phosphorylation and methylation, controls the de-repression of polycomb-silenced genes, whose temporally-regulated functions are crucial to development (Lau and Cheung, 2011). Conversely, nuclear-located histone deacetylases (HDACs) mediate the repression of gene transcription by the polycomb complex (Sadoul et al., 2010; Garrick et al., 2008).

Recent studies extended the view that reversible acetyl modification of proteins at internal lysine residues is not limited to events in the nucleus but also occurs in the cytoplasm, controlling important biological processes such as translation, cellular apoptosis, motility, and protein quality control (Creppe et al., 2009; Ctalano et al., 2007; Kim et al., 2006; Sadoul et al., 2010). For instance, αTAT1 is responsible for the acetylation of α-tubulin, whereas HDAC6 functions as a α-tubulin deacetylase exclusively in the cytoplasm (Shida et al., 2010; Hubbert et al., 2002). As a consequence, these modifications regulate microtubule stability, and thus cell motility, independent of both histone metabolism and gene transcription (Hubbert et al., 2002). While to date several hundreds of cytosolic proteins have been found to undergo an acetyl modification, the biological significance of this remains to be elucidated (Kim et al., 2006; Choudhary et al., 2009).

N-terminal acetylation is another enzyme-catalyzed reaction whereby N-terminal residues accept the acetyl group from acetyl-CoA. While it takes a place on approximately 80–90% of

* Corresponding authors. Tel./fax: +81 95 819 7017.
E-mail addresses: kyohyama@nagasaki-u.ac.jp (K. Ohyama), morinosm@nagasaki-u.ac.jp (N. Mori).

1567-133X/$ - see front matter © 2011 Elsevier B.V. All rights reserved.
doi:10.1016/j.gep.2011.11.001

cytosolic proteins in mammals, less attention has been paid to its function (Ametzazurra et al., 2008; Polevoda and Sherman, 2003; Polevoda et al., 2008, 2009). Emerging evidence suggests that an N-terminal acetylation of nascent polypeptides synthesized on polyribosomes plays a pivotal role in cellular homeostasis (Starheim et al., 2008; Arnesen et al., 2010). Based on *in vitro* studies, this modification has been proposed to influence protein function, stability, and subsequent modifications that include phosphorylation. It has been shown to control cell proliferation and protein quality to prevent the aggregation of abnormal proteins (Starheim et al., 2008; Arnesen et al., 2010). Biochemical studies have also shown that in the nervous system serotonin undergoes N-terminal acetyl modification and subsequent conversion to melatonin, thereby regulating the synthesis and metabolism of serotonin as a feedback system (Issac et al., 1990; Miguez et al., 1997; Sugiura et al., 2003). Nonetheless, due to the shortage of *in vivo* studies, it is still not well understood how N-terminal acetylation controls biological events in tissues.

N-acetyltransferase (Nat) complexes are composed of catalytic and auxiliary subunits, and are responsible for the enzymatic reaction to acetylate cytosolic proteins (Ametzazurra et al., 2008; Polevoda and Sherman, 2003; Polevoda et al., 2008, 2009). In yeast, five *N*-alpha-acetyltransferases (NATs), i.e. NatA-E, have been described as catalytic subunits, depending on the distinct amino acid sequences at N-termini they recognize. NatA, NatB, and NatC are three major *N*-acetyltransferases, whereas the substrates for NatD and E are poorly identified. As auxiliary subunits of three major Nat complexes (i.e. NatA, NatB, and NatC), Nat1p, Mdm20p, Mak31p have been identified, respectively in yeast.

In mammals, the NatA complex is composed of a catalytic subunit, ARD1 (arrested defective 1) and an auxiliary subunit NATH (*N*-acetyltransferase human). In the developing mouse brain, both ARD1 and NATH are highly expressed in proliferating progenitors and their expression is downregulated as they differentiate (Gendron et al., 2000; Sugiura et al., 2003). A recent study also showed that NatA complex ARD1-NAT1 is required for the dendritic arbolization of Purkinje cells in the postnatal cerebellum (Ohkawa et al., 2008). These studies clearly indicate that N-terminal acetyl-modification of proteins plays an important role in both the developing and mature brain.

Mdm20 (a regulator of mitochondrial distribution and morphology) is an auxiliary subunit of the NatB complex, the second major acetyltransferase and binds catalytic subunit Nat3 in yeast (Starheim et al., 2008; Ametzazurra et al., 2008; Polevoda and Sherman, 2003; Polevoda et al., 2009). The yeast NatB complex, Mdm20/Nat3 regulates tropomyosin-actin interactions (Singer and Shaw, 2003). In human cells, the NatB acetyltransferase complex is composed of Mdm20 and Nat5 (the human orthologue of yeast Nat3) and has been shown to be essential for cell cycle progression. (Starheim et al., 2008). Given that mouse Nat5 is the closest Nat family protein to human Nat5 and yeast Nat3, mMdm20 and mNat5 are likely to be the auxiliary and catalytic subunits of a mouse NatB acetyltransferase complex, respectively (Starheim et al., 2008; Ametzazurra et al., 2008; Polevoda and Sherman, 2003; Polevoda et al., 2008).

Although *in vitro* studies have suggested the importance of NatB complexes in fundamental cellular events, namely cell proliferation and cytoskeletal organization, none of the subunit proteins

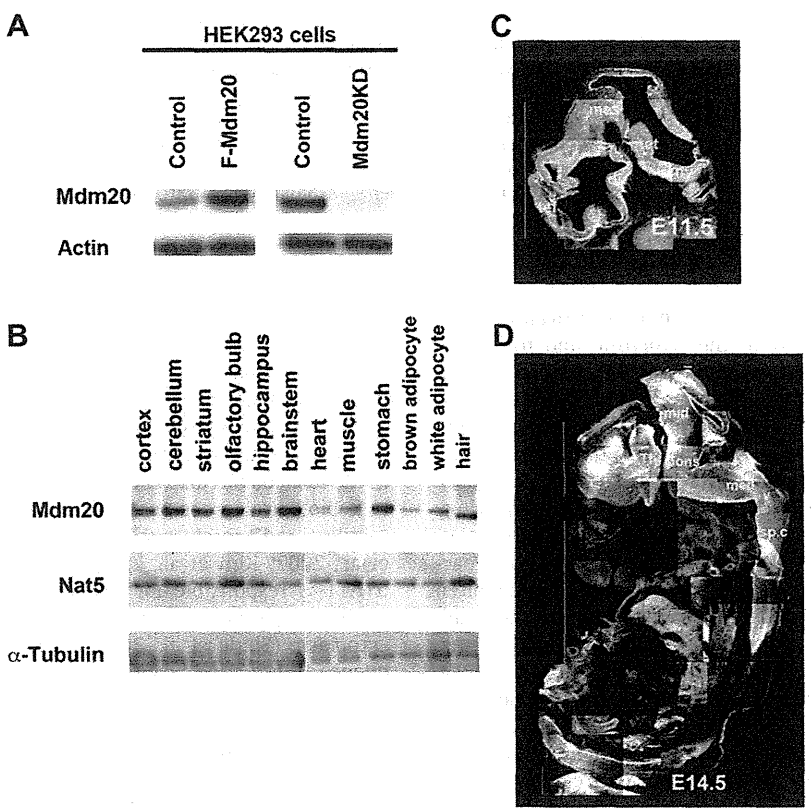

Fig. 1. Mdm20 is highly expressed in the embryonic and adult mouse brains. (A) Western blot of human embryonic kidney (HEK) 293 cells lysates using anti-Mdm20 rabbit polyclonal antibody. When a flag-tagged human Mdm20 was overexpressed (F-Mdm20), an increased expression of Mdm20 was detected. Conversely, an endogenous expression of human Mdm20 was decreased when human Mdm20 was knocked down by human Mdm20 siRNA (Mdm20KD). Western blot of β-actin was used as an internal control. (B) Western blot analysis of adult mouse tissues. Both Mdm20 and Nat5 are highly expressed in the brain (cerebral cortex, cerebellum, striatum, olfactory bulb, hippocampus, brainstem), stomach, and hair, compared to their expression level in heart and muscle. α-Tubulin expression was monitored as internal controls. (C and D) Immunofluorescent labeling of Mdm20 in mouse embryo at E11.5 (C) and E14.5 (D). Sagittal section of the mouse embryonic brain shows that Mdm20 is highly expressed in the brain and spinal cord. tel; telencephalon, mes; mesencephalon, dien; diencephalon, bs; brainstem, str; striatum, sp.c; spinal cord.

have been investigated for their function *in vivo*. In fact, the expression patterns of Mdm20 and Nat5 have not been examined systematically in multi-cellular organisms. Here we document for the first time the distribution pattern of Mdm20 protein in the developing mouse brain and compare it with that of Nat5. We further describe their subcellular localization and discuss their possible functions in the developing brain.

1. Results

1.1. Mdm20 is highly expressed both in the developing and adult mouse brain

We first generated a rabbit polyclonal antibody against a carboxy-terminal sequence of the Mdm20 protein conserved between human and mouse. Using human embryonic kidney (HEK) 293 cell lysates, we performed Western blot analysis of Mdm20 and detected a specific single band, which corresponds to the predicted molecular weight 120 kD (Fig. 1 and data not shown). The anti-Mdm20 antibody also detected either the increase or decrease of Mdm20 expression when Flag-tagged full length of Mdm20 cDNA (F-Mdm20) was overexpressed or Mdm20 was knocked down by siRNA for Mdm20 (Mdm20KD), respectively (Fig. 1A). These data confirmed the specificity of the anti-Mdm20 antibody.

We next examined the tissue distribution of Mdm20 protein in adult mice. Western blot analysis demonstrated that both Mdm20 and Nat5 were highly expressed in the brain, stomach, and hair (Fig. 1B). Similar to its prominent expression in the adult brain, Mdm20 was found to be highly expressed in the embryonic brain as evidenced by immunofluorescent staining (Fig. 1C and D). Mdm20 expression was also evident in dorsal root ganglia, muscles, chondrocytes, skin, and heart (data not shown).

1.2. Mdm20 and Nat5 expression in neural progenitors and differentiating neurons of mouse embryonic brain

As Mdm20 is a component of the NatB complex, we further investigated the expression pattern of Mdm20 and compared it with that of Nat5 in the developing mouse brain. At E11.5 Mdm20 was widely expressed, including in most proliferating cell nuclear antigen (PCNA)+ proliferating neural progenitors (Fig. 2A–F). By contrast, somewhat surprisingly, Nat5 expression was considerably more restricted, notably in only a subset of PCNA+ neural progenitors (Fig. 2A–F). Double labelling of Nat5 and Sox1/3 revealed that Nat5+ cells were Sox1/3+ neural progenitors (Fig. 3). Consistent with this, pulse labeling with BrdU revealed that Mdm20+ cells at the VZ were BrdU+ proliferating progenitors (Fig. 4A). Our data also showed that Mdm20+ cells in the mantle

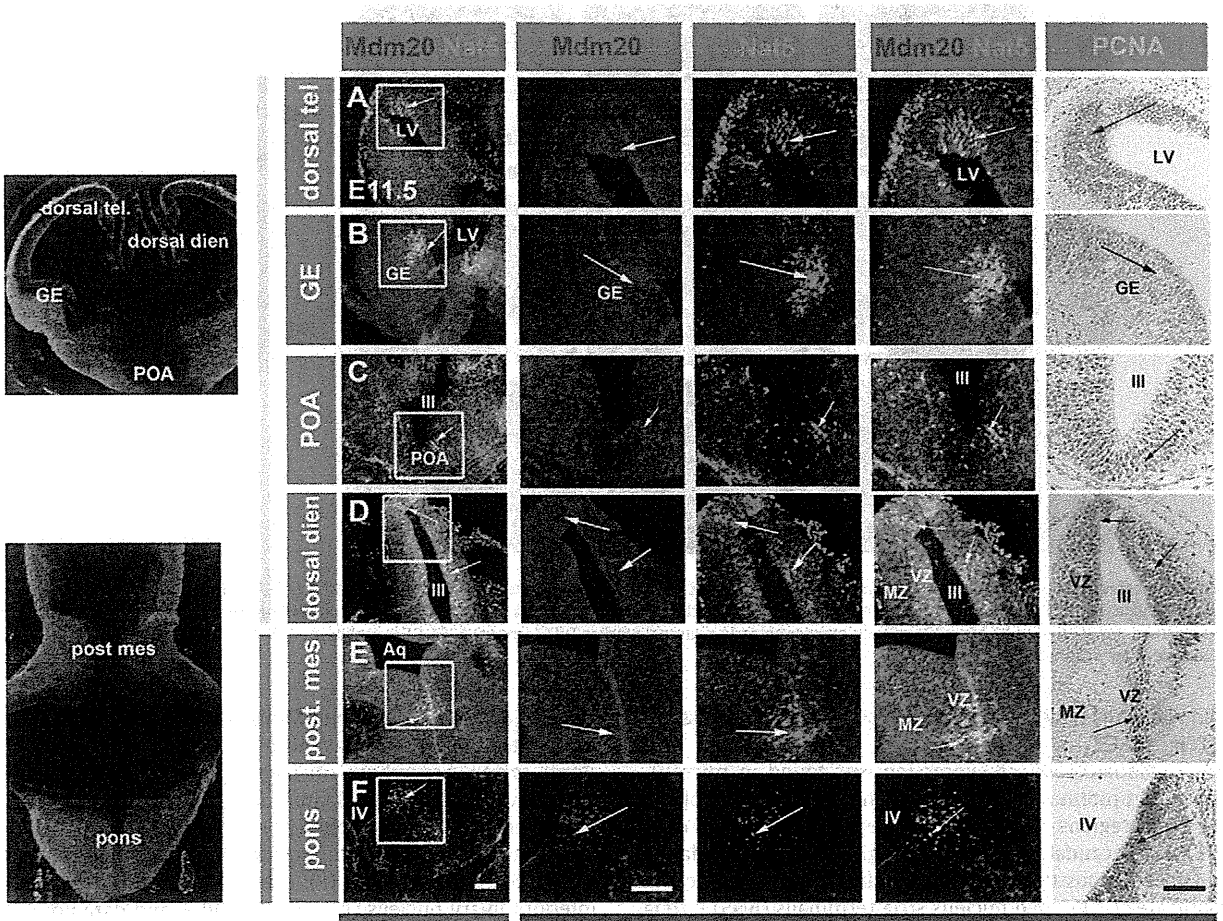

Fig. 2. Expression of Mdm20 and Nat5 in mouse embryonic brain at E11.5. (A–F) Transverse sections through the brain show a widely distributed expression of Mdm20 (red). In contrast, Nat5 expression (green) is restricted to subsets of proliferating cell nuclear antigen (PCNA)+ proliferating neural progenitors at the ventricular zones (VZ) of dorsal telencephalon (tel) (arrows in A), GE and POA in the ventral telencephalon (arrows in B and C), dorsal diencephalon (dien) (arrows in D), posterior mesencephalon (post mes) (arrows in E), and at the border between alar and basal plates of the pons (arrows in F). Nat5 expression was also found in the head mesenchyme. Left panels show TuJ1+ early neurons (green) at lower magnification of the brain tissues with DAPI counter stain (blue). Boxed regions were shown as at higher magnification. PCNA staining was performed at the equivalent levels but in different brain tissues from those for the analysis of Mdm20 and Nat5 expression. LV, lateral venricle; GE, ganglionic eminence; III, the third ventricle; VZ, ventricular zone; MZ, mantle zone; POA, preoprtic area; Aq, aqueduct; IV, the fourth ventricle. Scale bars: 30 μm.

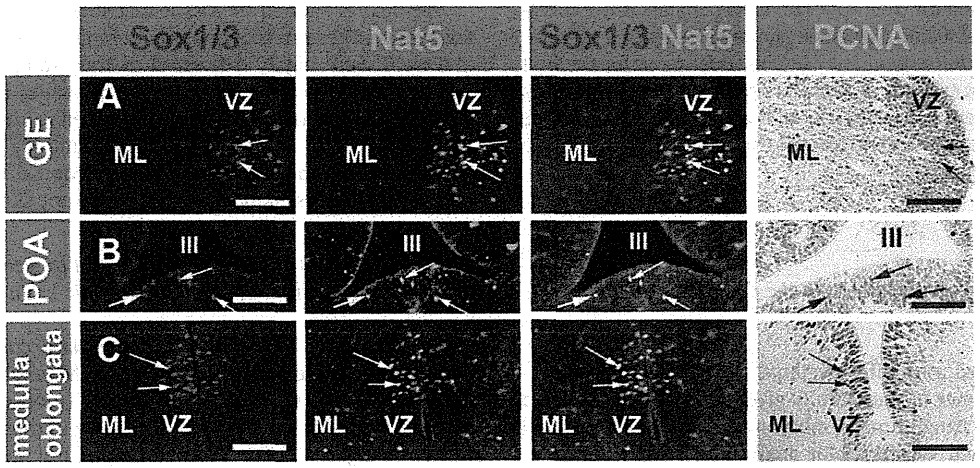

Fig. 3. Nat5 expression in Sox1/3+ neural progenitors at E12.5. (A–C) Transverse sections through the ganglionic eminence (GE), preoptic area (POA), and medulla oblongata at E12.5. Co-expression of Sox1/3 and Nat5 is found in PCNA+ proliferating progenitors at the VZ of the GE, POA, and medulla oblongata (arrows in A–C). GE, ganglionic eminence; POA, preoprtic area; VZ, ventricular zone; ML, mantle layer. III, the third ventricle. Scale bars: 30 μm

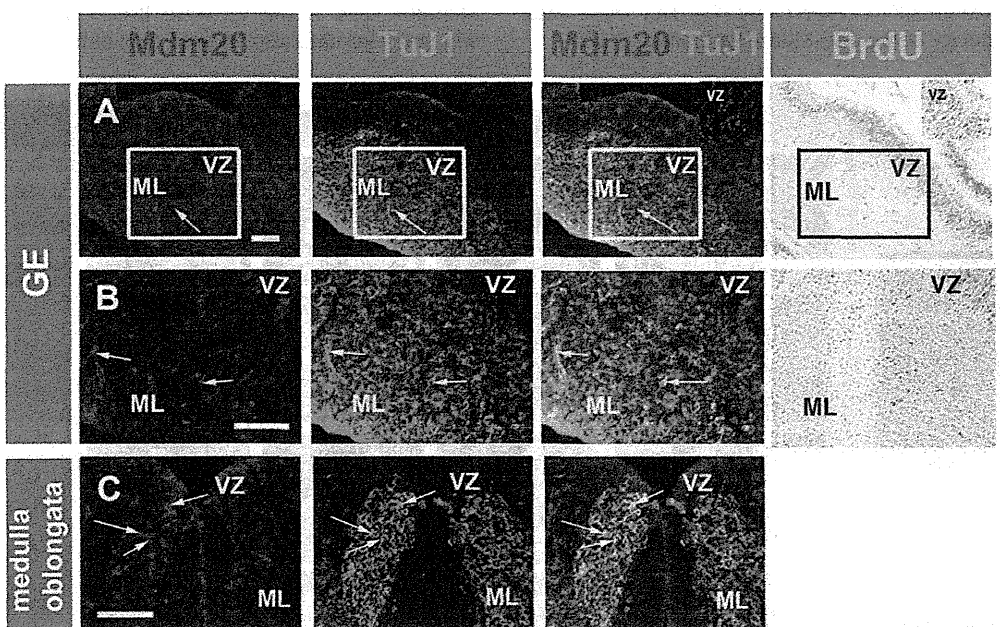

Fig. 4. Mdm20 is expressed in both proliferating neural progenitors at the VZ and TuJ1+ early differentiating neurons at E12.5. (A–C) Transverse sections through the GE and the medulla oblongata. Mdm20 is expressed both in the VZ and ML of both the GE and the medulla oblongata (A–C). Bromodeoxy-uridine (BrdU) pulse-labeled cells for 1hr are located mostly in the VZ (A and B). Mdm20+ cells co-express an early neuronal marker TuJ1 (arrows, A–C). GE, ganglionic eminence; POA, preoprtic area; VZ, ventricular zone; ML, mantle layer. Scale bars: 30 μm.

layer (ML) were TuJ1+, indicating that they are early differentiating neurons (Fig. 4A–C).

By E14.5, Mdm20/Nat5 co-expression was found in microtubule-associated protein 2 (MAP2)+ differentiating neurons of the following brain regions: olfactory bulb, septum, ganglionic eminence (GE) and its caudal part, CGE, which gives rise to amygdaloid neurons. Other regions that co-express Mdm20 and Nat5 include the preoptic area (POA), bed nucleus stria terminalis (BNST), zona incerta (Zi), epithalamus (Epith), dorsal raphe (DR), principal sensory nucleus of trigeminal nerves (Pr5s), vestibular nucleus, cochlear, external cuneate nucleus (EC), medullary raphe (Ra), spinal trigeminal nucleus (Sp5n) and so on (Figs. 5 and 6). It is noteworthy that cerebellar deep neurons express Mdm20 but not Nat5 (Fig. 6E), indicating the existence of Mdm20+/Nat5− cells in the brain.

At E18.5, co-expression of Mdm20/Nat5 was maintained in differentiated neurons such as those in the septum, pineal gland, piriform cortex, accumbens nucleus (NAc), Zi, amygdala, cingulate cortex, ventral tegmental area, interpeduncular nucleus, dorsal raphe, and medullary raphe (Ra) containing serotonergic (5-HT) neurons, spinal trigeminal nucleus (Pr5n), cochlear nucleus, pontine reticular formation (RF), external cuneate nucleus (EC), and inferior olivary nucleus (IO) (Figs. 7 and 9, and data not shown).

1.3. Mdm20 is not necessarily co-expressed with Nat5 in the developing mouse brain

At early stages of neurogenesis (E11.5–12.5), the majority of neural progenitors at the VZ that express Mdm20 do not co-express Nat5 (Fig. 2). Similarly, while a vast majority of Nat5+

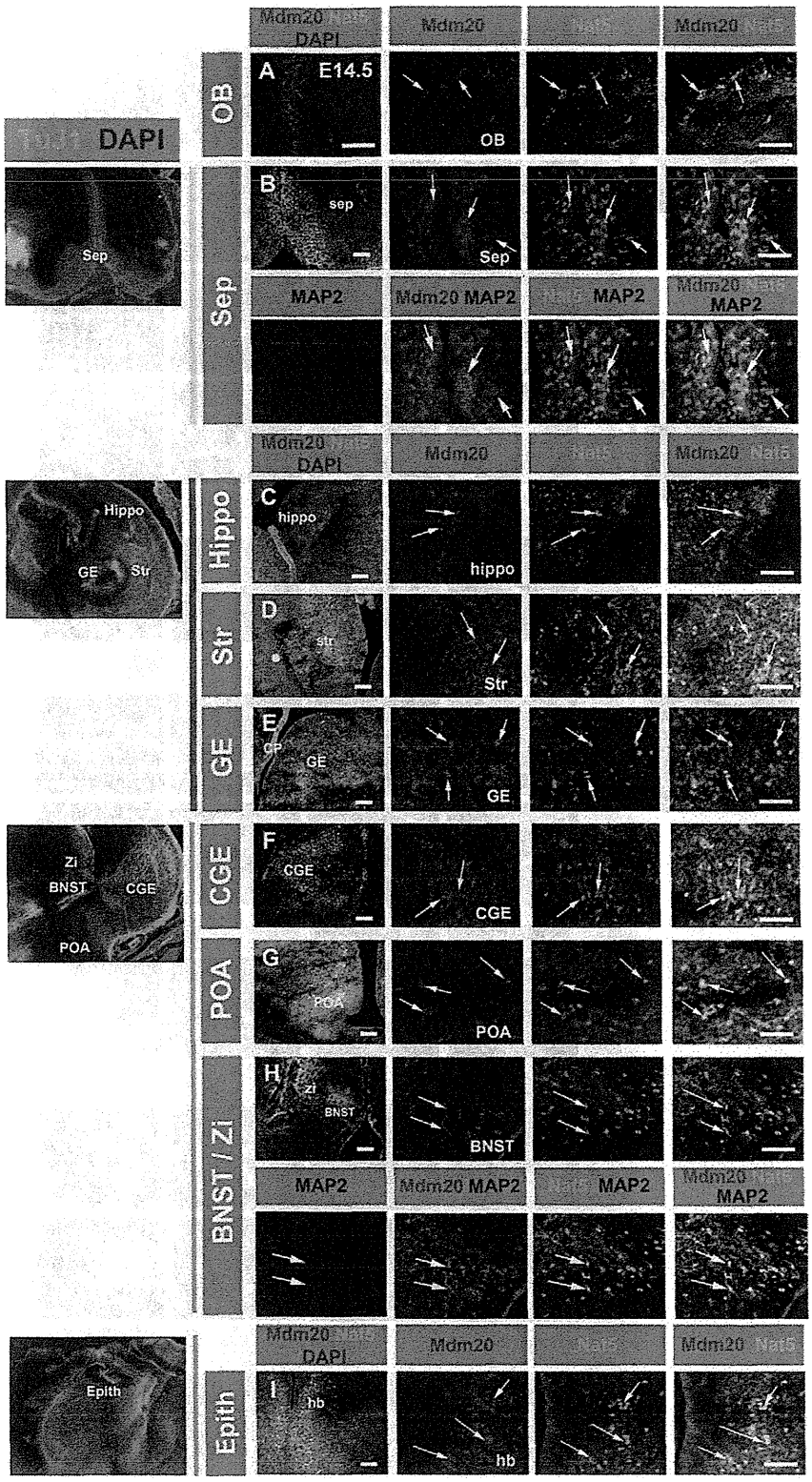

Fig. 5. Expression of Mdm20 and Nat5 in differentiating neurons of mouse embryonic forebrain at E14.5. (A–I) Transverse sections through the mouse forebrain at E14.5. Co-expression of Mdm20 and Nat5 is found in differentiating neurons of the following forebrain regions (arrows) in A–I: (A) olfactory bulb (OB); (B) septum (Sep); (C) hippocampus (Hippo); (D) striatum (Str); (E) ganglionic eminence (GE); (F) caudal ganglionic eminence (CGE); (G) preoptic area (POA); (H) bed nucleus stria terminalis (BNST)/zona incerta (Zi); epithalamus (Epith). Left panels show TuJ1+ early neurons (green) at lower magnification of the brain regions counterstained with DAPI (blue). Co-expression of Mdm20, Nat5, and neuronal marker MAP2 was found in the Sep (arrows in B) and BNST (arrows in H). Scale bars:30 μm on the left column of A–I; 15 μm on the three columns of A-I from the right, showing pictures at a higher magnification.

differentiating neurons co-express Mdm20 at E14.5 and onward, Mdm20+/Nat5− neurons were also observed in the brain regions such as facial nucleus, preoptic area (POA), thalamic paraventricular nucleus (Th PVN), lateral reticular nucleus (LRN), and cerebellar

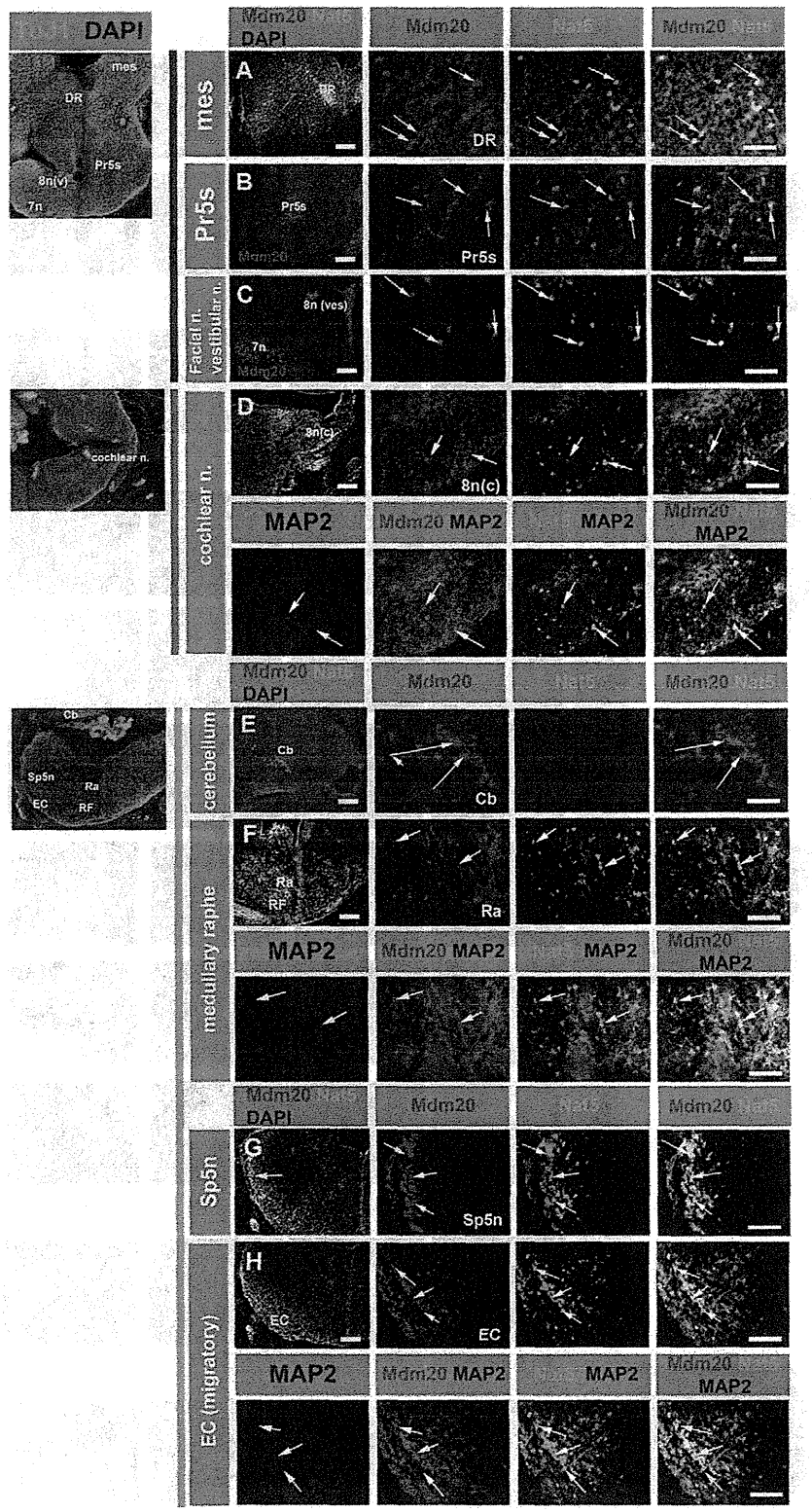

Fig. 6. Mdm20 and Nat5 expression in differentiating neurons of mouse brainstem at E14.5. (A–H) Transverse sections through the mouse brainstem at E14.5. (A–D) Co-expression of Mdm20 (red) and Nat5 (green) in the upper brainstem (arrows): (A) dorsal raphe in the mesencephalon (DR); (B) principal sensory trigeminal nucleus (Pr5s); (C) vestibular nucleus, Note that facial neurons does not express Nat5; (D) cochlear neurons. (E–H) Expression of Mdm20 (red) and Nat5 (green) in the lower brainstem and cerebellum (arrows): (E) cerebellar deep neurons (Cb); (F) medullary raphe neurons (Ra); reticular formation (RF); (G) spinal trigeminal neurons (Sp5n) (arrows); (H) migratory external cuneate neurons (EC) (arrows). Note that cerebellar deep neurons express Mdm20 but not Nat5. Left panels show TuJ1+ early neurons (green) at lower magnification of the brain regions stained wih DAPI (blue). Co-expression of Mdm20, Nat5, and neuronal marker MAP2 was found in the cochlear nucleus (arrows in D), RF (arrows in F), and EC (arrows in H). Scale bars: 30 μm on the left column of A–H; 15 μm on the three columns of A–H from the right, showing pictures at a higher magnification.

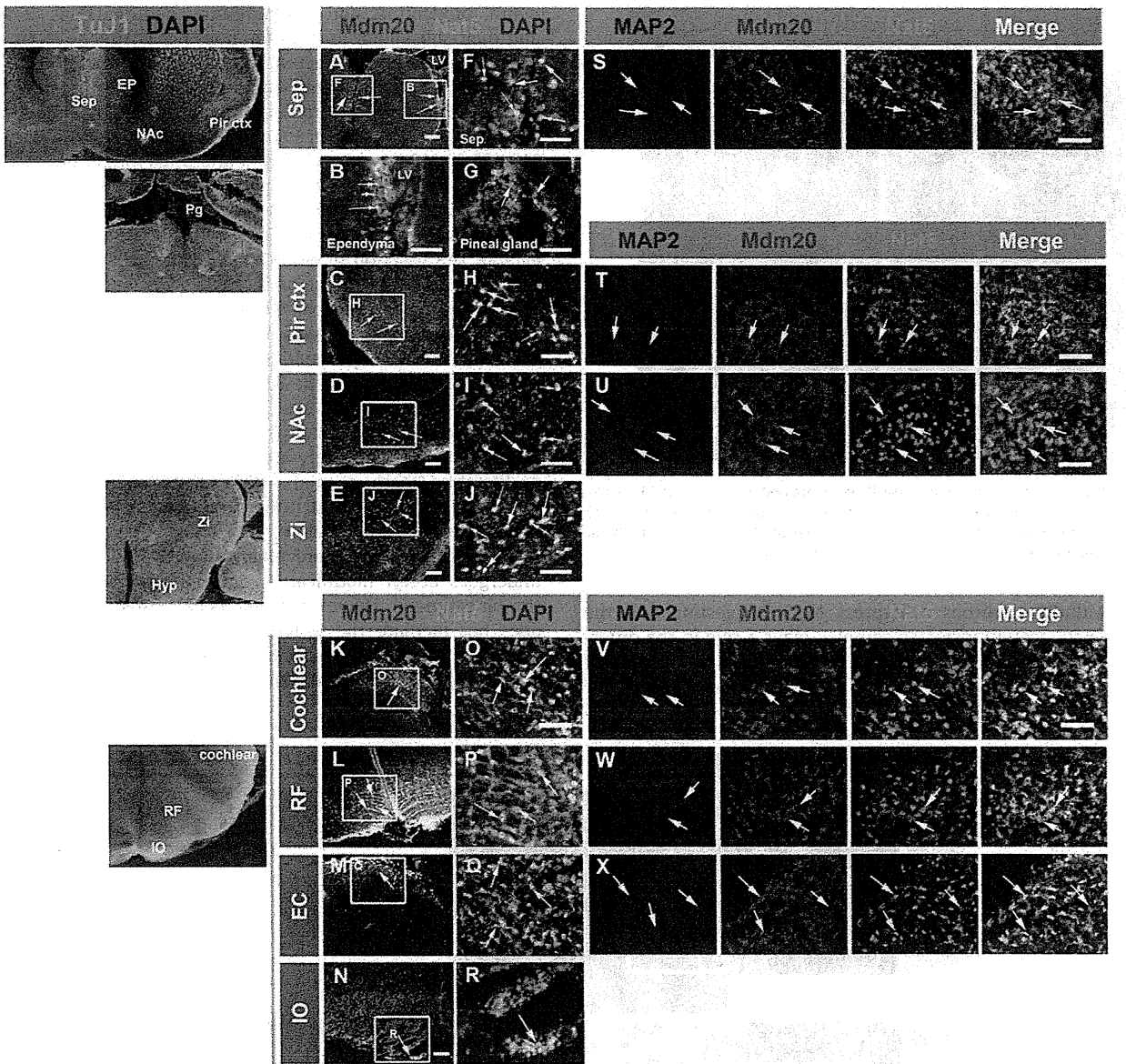

Fig. 7. Mdm20 and Nat5 are co-expressed in differentiated neurons at E18.5. (A–R) Transverse sections through the brain. Co-expression of Mdm20 and Nat5 is found in the septum (arrows in A and F), ependymal cells facing at the lateral ventricle (LV) (arrows in B), piriform cortex (Pir ctx) (arrows in C and H), accumbens nucleus (NAc) (arrows in D and I), zona incerta (Zi) (arrows in E and J), pineal gland (Pg) (arrows in G), cochlear nucleus (arrows in K and O), potine reticular formation (RF) (arrows in L and P), EC (arrows in M and Q), and the ventral portion of inferior olivary nucleus (IO) (arrows in N and R). Left panels show TuJ1+ neurons (green) at a lower magnification of the brain regions stained wih DAPI (blue). hyp; hypothalamus. Co-expression of Mdm20, Nat5, and neuronal marker MAP2 was found in the Sep (arrows in S), Pir ctx (arrows in T), NAc (arrows in U), cochlear nucleus (arrows in V), RF (arrows in W), and EC (arrows in X). Scale bars: 30 μm in A, C, D, E, K–N; 15 μm in B, F-J, O–X.

deep neurons (Figs. 6C and E and 8A–D). Moreover, although vestibular neurons (Ves) co-express Mdm20 and Nat5 at E14, the downregulation of Nat5 occurs in the Ves by E18.5 (Figs. 6C and 8B). These data indicate that the expression of Mdm20 and Nat5 is not only spatially regulated but also changes over time.

Although Mdm20 and Nat5 were found to co-express in the midbrain DA neurons *in vivo* (Fig. 9A–C), we also noted that their subcellular localization appeared to be distinct (Fig. 9A and B). Mdm20 was mainly localized in the cytoplasm, whereas Nat5 was found in the nucleus. This data is consistent with the previous observation using cultured tumor cells (Starheim et al., 2008), although they showed some co-localization of Mdm20 and Nat5 in the cytoplasm. To clarify the subcellular localization of Mdm20 and Nat5 in neurons, we monitored their expression in the midbrain DA neurons cultured *in vitro*. The midbrain was isolated from E18.5 rat embryos and cultured for 2–4 weeks. Expression of Mdm20 and Nat5 was assessed by an immunofluorescent labeling experiment. Consistent with *in vivo* data (Fig. 9A–C), Mdm20 was mainly localized in the cytoplasm especially in the perinuclear region of tyrosine hydroxylase (TH)+ DA neurons, whereas Nat5 was mainly in the nucleus (Fig. 9D–G).

2. Discussion

In the present study, we have documented the spatial and temporal expression pattern of Mdm20 in comparison with that of Nat5 in the developing mouse brain. Mdm20 is highly expressed in the developing mouse brain. Early on, it is widely distributed in neural progenitors (Figs. 1–4). As development proceeds, Mdm20 expression is downregulated in proliferating progenitors and found in differentiating neurons (Figs. 5–7). The vast majority

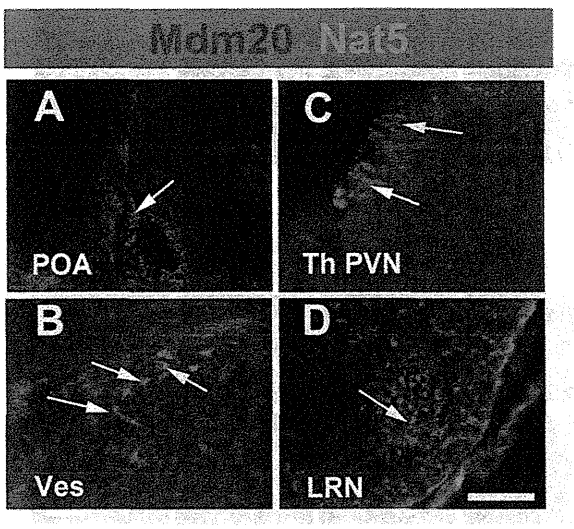

Fig. 8. Mdm20 and Nat5 are not necessarily co-expressed in neurons at E18.5. (A–D) Transverse sections through the brain at E18.5. Mdm20 (red) but not Nat5 (green) is found in (A) the preoptic area (POA) (A), vestibular nucleus (B), thalamic paraventricular nucleus (Th PVN) (C), and lateral reticular nucleus (D). Scale bars: 30 μm.

of the Mdm20+ neurons co-express Nat5, suggesting that the Mdm20/Nat5 acetyltransferase complex plays a role in the differentiation of neurons. Careful analysis of the expression pattern of Mdm20 and Nat5 also reveals the existence of Mdm20+/Nat5– neural progenitors and differentiating neurons (Figs. 2 and 8), and their subcellular localization does not entirely overlap in differentiated neurons as seen in midbrain DA neurons (Fig. 9).

Previous studies of yeast and human cells *in vitro* showed that Mdm20 controls cell proliferation and actin dynamics (Singer and Shaw, 2003; Starheim et al., 2008). Consistent with this notion, Mdm20 is widely expressed in neural progenitors (at E11.5–12.5) (Figs. 1 and 2). Given that cell polarity of neural progenitors is crucial to control the number of neural progenitors and their differentiation (Huttner and Kosodo, 2005), further studies are needed to explore the function of Mdm20 in proliferating progenitors and their differentiation in the brain.

Our data has also revealed that both Mdm20 and Nat5 expression changes in space and time. Intriguingly, by E14.5, both Mdm20 and Nat5 expression is downregulated in most of the proliferating progenitors at the VZ and becomes restricted to postmitotic differentiating neurons (Figs. 5 and 6). Our observation of Nat5/Mdm20 co-expression in Sox1/3+ proliferating neural progenitors supports a widely accepted role for Mdm20/Nat5 in cell proliferation (Starheim et al., 2008). Moreover, our data imply that Mdm20/Nat5 has an unidentified additional role in differentiating neurons as we discuss below.

Biochemical studies previously showed that serotonin (5-HT) undergoes acetyl modification and conversion to melatonin in the pineal gland. However, it has been shown that Nat1/NATH1 does not mediate the *N*-acetylation of serotonin (Heim et al., 1991). In the present study, we found that Mdm20 and Nat5 are co-expressed in the pineal gland (Fig. 7G). It raises a possibility that

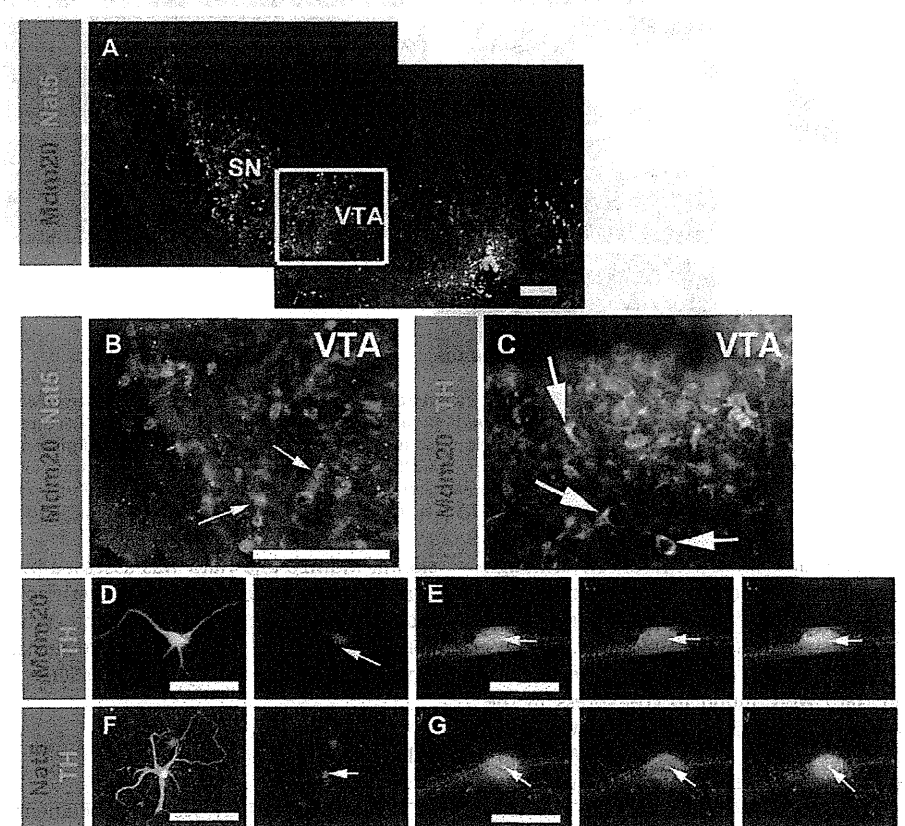

Fig. 9. Subcellular localization of Mdm20 and Nat5 protein in midbrain DA neurons. (A–C) Mdm20 (red) and Nat5 (green) are co-expressed in tyrosine hydroxylase (TH)+ dopaminergic (DA) neurons at the substantia nigra (SN) and the ventral tegmental area (VTA) in mouse midbrain (arrows). (D–I) Subcellular localization of Mdm20 (red) and Nat5 (red) in the rat midbrain DA neurons (green) cultured *in vitro*. To clarify the subcellular localization of both Mdm20 and Nat5, cell nuclei were visualized by DAPI staining (blue in E and G). Mdm20 (red) is mainly localized in the cytoplasm especially in the perinuclear region of the TH + DA neurons (arrows in D and E; note that Mdm20 is localized at the vicinity of DAPI+ cell nucleus), whereas Nat5 (red) is in the nucleus (arrows in F and G; note that Nat5 expression is overlapped with DAPI+ cell nucleus). Scale bars: 30μm in A–D, F; 5 μm in E and G.

the Nat5/Mdm20 complex contributes to the conversion of serotonin to melatonin in the gland, which needs to be tested in the future experiments.

More intriguingly, another possible role for Mdm20 and Nat5 is to control cellular survival and ageing (Liu et al., 2010; Arnesen et al., 2010), and we assume such a role should be very important in postmitotic cells, e.g. neurons. An assembly of actin cables is crucial for controlling cell polarity, and a tropomyosin-dependent polarized retrograde transport of protein aggregates along the actin cables is an important process for proteostasis (Liu et al., 2010). This process is mediated by a protein complex called a polarisome, which could be associated with Mdm20. As these processes are crucial to prevent the senescence of budding yeast (Liu et al., 2010), we assume that Mdm20 may play a similar role in protein clearance in mature and/or aging neurons, and thus their survival. To support the notion, a recent study showed that a chaperone-like protein HYPK physically interacts with NatA, preventing Huntingtin aggregation (Arnesen et al., 2010). It is conceivable that, after becoming post-mitotic, neurons possess a cellular machinery by which they tightly regulate a protein quality for their survival throughout life. As the expression of Mdm20/Nat5 continues into adulthood, Mdm20 may play a role in protein clearance or metabolism in the long life of post-mitotic neurons.

In addition to the co-expression of Mdm20 and Nat5, our data clearly indicate the existence of Mdm20+/Nat5− neurons. Our data show that differential expression of Mdm20 and Nat5 is achieved in three different ways: (1) spatially distinct expression of Nat5 and Mdm20; (2) temporal downregulation of Nat5 in Mdm20+ cells; (3) different subcellular localization of Mdm20 and Nat5. A previous study suggested that Mdm20 and Nat5 have functions other than those as a Mdm20/Nat5 complex in human cells (Starheim et al., 2008). Given that mNat5 is currently only one possible example of the Nat protein family that interacts with Mdm20 (Singer and Shaw, 2003; Polevoda and Sherman, 2003), our data imply that Mdm20 may function with some unidentified Nat proteins and/or in a Nat-independent manner.

3. Experimental procedures

3.1. Animals

All experiments were carried out according to the guidelines established by the Animal Welfare Committee of Nagasaki University. Pregnant wild-type C57BL/6J mice and rats were sacrificed by cervical dislocation under deep anesthesia with diethyl ether. Mouse and rat embryos were harvested at E11.5–18.5 and E18.5, respectively. They were processed for immunohistochemistry or culture experiments as described in the following Sections 3.3 and 3.4.

3.2. Antibody generation and Western blot analysis

A rabbit polyclonal antibody was generated against C-terminal peptides, LEDTSLSPEERKFSKTVQGKVQSSYLHSLLEMGELLKKRLETTKKLKI of human Mdm20 protein, which is conserved between human and mouse, fused with GST protein. The antiserum was purified by GST column and protein A sepharose. Western blot analysis of adult mouse tissues (20 μg of protein per lane) was carried out as described previously (Mori-Konya et al., 2009). Flow through fraction of antiserum with GST column did not detect the 120 kD band, confirming the specificity of the anti-Mdm20 antibody generated. Western blots of either α-tubulin or β-actin were used as internal controls. Mdm20 was knocked down by siRNA (Mdm20KD), whose target sequence was the 329–248 nucleotide sequence of human Mdm20 gene.

3.3. Immunohistochemistry

Mouse embryonic brains (C57BL/6J; $n = 5–8$ for each stages examined) were fixed in 4% paraformaldehyde (PFA) for 2–6 h depends on their age. After washing with PBS, tissues were immersed in 30% sucrose/0.1 M phosphate buffer (PB). Cryosections were incubated with antibodies as described previously (Ohyama et al., 2004, 2005). Pulse labeling with BrdU for 1 h was performed as described previously (Ohyama et al., 2004). Following antibodies were used: rabbit anti-Mdm20 polyclonal antibody (1:250); goat polyclonal anitibody against Nat5 (Santa Cruz, CA, USA, 1:25–100); TuJ1 mouse IgG (Covance, Japan, 1:1000); mouse anti-PCNA (Novocastra, U.K., 1:100); rabbit anti-Sox1/3 (1:1000, gift of H. Kondo); mouse anti-BrdU (Becton Dickinson, NJ, USA, 1:50–100); mouse anti-TH monoclonal antibody (Sigma, 1:2000); mouse anti-MAP2 (Sigma-Aldrich, MO, USA, 1:500–1000); Alexa 567 donkey anti-rabbit IgG (Molecular probes, USA, 1:500); Alexa 488 donkey anti-goat IgG (Molecular probes, USA, 1:500); Alexa 488 donkey anti-mouse IgG (Molecular probes, USA, 1:500); Alexa 305 anti-mouse IgG (Molecular probes, USA, 1:500); HRP-conjugated anti mouse IgG. Images were captured using fluorescent and confocal microscope (Carl Zeiss Axioskop2 plus; Carl Zeiss Axiovert200M LSM510) with an Axiovision software and BIOREVO BZ-8100 imaging system (Keyence, Osaka, Japan). Primary antibody incubation was omitted for negative control experiments. The specificity of Nat5 immunoreactivity was also confirmed by neurtralization with blocking peptide (Santa Cruz, CA, USA) following a manufacturer's instruction. The specificity of anti-Mdm20 sera was also confirmed by neutralization with purified Mdm20 antigen (data not shown).

3.4. In vitro culture of midbrain DA neurons

Embryonic midbrain tissues were isolated from pregnant rats (Sprague Dawley) at E18.5, and were cultured using a standard protocol as described previously for hippocampal neurons (Morii et al., 2006).

Acknowledgements

We thank Dr. H. Kondo (Osaka University, Japan) for anti-Sox1/3 antibody, Dr. S. Hori (Kyoto University, Japan) for preparing purified Mdm20 protein, Drs. A. Furley and P. Ellis (University of Sheffield, UK) for their critical reading of the manuscript. This work was supported by Grants-in-Aid for Scientific Research from MEXT Japan (Kiban B) (to N.M.), and also, in part, by Asian CORE program of JSPS (to N.M.), and a Start-up fund for new investigators from Nagasaki University (to K.O.).

References

Ametzazurra, A., Larrea, E., Civeira, M.P., Prieto, J., Aldabe, R., 2008. Implication of human N-α-acetyltransferase 5 in cellular proliferation and carcinogenesis. Oncogene 27, 7296–7306.

Arnesen, T., Van Damme, P., Polevoda, B., Helsens, K., Evjenth, R., Colaert, N., Varhaug, J.E., Vandekerckhove, J., Lillehaug, J.R., Sherman, F., Gevaert, K., 2009. Proteomics analyses reveal the evolutionary conservation and divergence of N-terminal acetyltransferase from yeast and human. Proc. Natl. Acad. Sci. U S A. 19, 157–162.

Arnesen, T., Starheim, K.K., Van Damme, P., Evjenth, R., Dinh, H., Betts, M.J., Ryningen, A., Vandekerckhove, J., Gevaert, K., Anderson, D., 2010. The chaperone-like protein HYPK acts together with NatA in cotranslational N-terminal acetylation and prevention of Huntingtin aggregation. Mol. Cell. Biol. 30, 1898–1909.

Choudhary, C., Kumar, C., Gnad, F., 2009. Lysine acetylation targets protein complexes and co-regulates major cellular functions. Science 325, 834–840.

Creppe, C., Makinouskaya, L., Volvert, M.-L., Gillard, M., Close, P., Malaise, O., Laguesse, S., Cornez, I., Rahmouni, S., Ormenese, S., Belachew, S., Malgrange, B., Chapelle, J.-P., Siebenlist, U., Moonen, G., Chariot, A., Mguyen, L., 2009. Elongator

controls the migration and differentiation of cortical neurons through acetylation of α-tubulin. Cell 136, 551–564.
Ctalano, M.G., Poli, R., Pugliese, M., Fortunati, N., Boccuzzi, G., 2007. Valproic acid enhances tubulin acetylation and apoptotic activity of paclitaxel on anaplastic thyroid cancer cell lines. Endocrine-Related Cancer 14, 839–845.
Dessaud, E., Yang, L.L., Hill, K., Cox, B., Ulloa, F., Ribeiro, A., Mynett, A., Novitch, B.G., Briscoe, J., 2007. Interpretation of the sonic hedgehog morphogen gradient by a temporal adaptation mechanism. Nature 450, 717–720.
Garrick, D., De Gobbi, M., Samara, V., Rugless, M., Holland, M., Ayyub, H., Lower, K., Sloane-Stanley, J., Gray, N., Koch, C., Dunham, I., Higgs, D.R., 2008. The role of the polycomb complex in silencing α-globulin gene expression in nonerythroid cells. Blood 112, 3889–3899.
Gendron, R.L., Adams, L.C., Paradis, H., 2000. Tubedown-1, a novel acetyltransferase associated with blood vessel development. Dev. Dyn. 218, 300–315.
Heim, M.H., Blum, M., Beer, M., Meyer, U.A., 1991. Acetylation of serotonin in the rabbit pineal gland: an *N*-acetyltransferase with properties distinct from NAT1 and NAT2 is responsible. J. Neurochem. 57, 1095–1099.
Hubbert, C., Guardiola, A., Shao, R., Kawaguchi, Y., Ito, A., Nixon, A., Yoshida, M., Wang, X.-F., Yao, T.-P., 2002. HDAC6 is a microtubule-associated deacetylase. Nature 417, 455–458.
Huttner, W.B., Kosodo, Y., 2005. Symmetric versus asymmetric cell division during neurogenesis in the developing vertebrate central nervous system. Curr. Opin. Cell Biol. 17, 648–657.
Issac, R.E., Muimo, R., MacGregor, A.N., 1990. N-Acetylation of serotonin, octopamine and dopamine by adult Brugia pahangi. Mol. Biochem. Parasitol. 43, 193–198.
Kim, S.C., Sprung, R., Chen, Y., et al., 2006. Substrate and functional diversity of lysine acetylation revealed by a proteomics survey. Mol. Cell 23, 607–618.
Kouzarides, T., 2000. Acetylation: a regulatory modification to rival phosphorylation? EMBO J. 19, 1176–1179.
Lau, P.N.L., Cheung, P., 2011. Histone code pathway involving H3 S28 phosphorylation and K27 acetylation activates transcription and antagonizes polycomb silencing. Proc. Natl. Acad. Sci. 108 (7), 2801–2806.
Liu, B., Larsson, L., Caballero, A., Hao, X., Oling, D., Grantham, J., Nystrom, T., 2010. The polarisome is required for segregation and retrograde transport of protein aggregates. Cell 140, 257–267.
Magalon, H., Patin, E., Austerlitz, F., Hegay, T., Aldashev, A., Quintana-Murci, L., Heyer, E., 2008. Population genetic diversity of the NAT2 gene supports a role of acetylation in human adaptation to farming in central asia. Eur. J. Hum. Genet. 16, 243–251.
Miguez, J.M., Martin, F.J., Aldegunde, M., 1997. Melatonin effects on serotonin synthesis and metabolism in the striatum, nucleus accumbens, and dorsal and median raphe nuclei of rats. Neurochem. Res. 22, 87–92.
Mori-Konya, C., Kato, N., Maeda, R., Yasuda, K., Higashimae, N., Noguchi, M., Koike, M., Kimura, Y., Ohizumi, H., Hori, S., Kakizuka, A., 2009. P97/valosin-containing protein (VCP) is highly modulated by phosphorylation and acetylation. Genes Cells 14, 483–497.
Morii, H., Shiraishi-Yamaguchi, Y., Mori, N., 2006. SCG10, a microtubule destabilizing factor, stimulates the neurite outgrowth by modulating microtubule dynamics in rat hippocampal primary cultured neurons. J. Neurobiol. 66, 1101–1114.
Ohkawa, N., Sugisaki, S., Tokunaga, E., Fujitani, K., Hayasaka, T., Setou, M., Inokuchi, K., 2008. *N*-acetyltransferase ARD1-NAT1 regulates neuronal dendritic development. Genes to Cells 13, 1171–1183.
Ohyama, K., Ikeda, E., Kawamura, K., Maeda, N., Noda, M., 2004. Receptor-like protein tyrosine phosphatase ζ/RPTPβ is expressed on tangentially aligned neurons in early mouse neocortex. Dev. Brain Res. 148, 121–127.
Ohyama, K., Ellis, P., Kimura, S., Placzek, M., 2005. Directed differentiation of neural cells to hypothalamic dopaminergic neurons. Development 132, 5185–5197.
Ohyama, K., Das, R., Placzek, M., 2008. Temporal progression of hypothalamic patterning by a dual action of BMP. Development 135, 3325–3331.
Pearson, C.A., Ohyama, K., Manning, L., Aghamohammadzadeh, S., Sandg, H., Placzek, M., 2011. FGF-dependent midline-deerived progeitor cells in hypothalamic infundibular development. Development 138, 2613–2624.
Polevoda, B., Sherman, F., 2003. Composition and function of the eukaryotic N-terminal acetyltransferase subunits. Biochem. Biophy. Res. Comm. 308, 1–11.
Polevoda, B., Brown, S., Cardillo, T.S., Rigby, S., Sherman, F., 2008. Yeast Nα-terminal acetyltransferases are associated with ribosomes. J. Cell. Biochem. 103, 492–508.
Polevoda, B., Arnesen, T., Sherman, F., 2009. A synopsis of eukaryotic Nα-terminal acetyltransferases: nomenclature, subunits and substrates. BMC Proc. (Suppl. 6), S2.
Sadoul, K., Wang, J., Diagouraga, B., Khochbin, S., 2010. The tale of protein lysine acetylation in the cytoplasm. J. Biomed. Biotech., 1–15, 970382.
Shida, T., Cueva, J.G., Xu, Z., Goodman, M.B., Nachury, M.V., 2010. The major α-tubulin K40 acetyltransferase α TAT1 promotes rapid ciliogenesis and efficient mechanosensation. Proc. Natl. Acad. Sci. 107, 21517–21522.
Sims 3rd, R.J., Reinberg, D., 2008. Is there a code embedded in proteins that is based on post-translational modifications? Nat. Reviews Mol Cell Biol. 9, 1–6.
Singer, J.M., Shaw, J.M., 2003. Mdm20 protein functions with Nat3 protein to acetylate Tpm1 protein and regulate tropomyosin-actin interactions in budding yeast. Proc. Natl. Acad. Sci. USA 100, 7644–7649.
Starheim, K.K., Arnsen, T., Gromyko, D., Ryningen, A., Varhaug, J.E., Lillehaug, J.R., 2008. Identification of the human Nα-acetyltransferase complex B (hNatB): a complex important for cell-cycle progression. Biochem. J. 415, 325–331.
Sugiura, N., Adams, S.M., Corriveau, R.A., 2003. An evolutionarily conserved N-terminal acetyltransferase complex associated with neuronal development. J. Biol. Chem. 278, 40113–40120.

Real-Time Imaging of Rabbit Retina with Retinal Degeneration by Using Spectral-Domain Optical Coherence Tomography

Yuki Muraoka[1], Hanako Ohashi Ikeda[1]*, Noriko Nakano[1], Masanori Hangai[1], Yoshinobu Toda[2], Keiko Okamoto-Furuta[2], Haruyasu Kohda[2], Mineo Kondo[3], Hiroko Terasaki[4], Akira Kakizuka[5], Nagahisa Yoshimura[1]

1 Department of Ophthalmology and Visual Sciences, Kyoto University Graduate School of Medicine, Kyoto, Japan, **2** Center for Anatomical Studies, Kyoto University Graduate School of Medicine, Kyoto, Japan, **3** Department of Ophthalmology, Mie University School of Medicine, Tsu, Japan, **4** Department of Ophthalmology, Nagoya University Graduate School of Medicine, Nagoya, Japan, **5** Laboratory of Functional Biology, Kyoto University Graduate School of Biostudies and Solution Oriented Research for Science and Technology, Kyoto, Japan

Abstract

Background: Recently, a transgenic rabbit with rhodopsin Pro 347 Leu mutation was generated as a model of retinitis pigmentosa (RP), which is characterized by a gradual loss of vision due to photoreceptor degeneration. The purpose of the current study is to noninvasively visualize and assess time-dependent changes in the retinal structures of a rabbit model of retinal degeneration by using speckle noise-reduced spectral-domain optical coherence tomography (SD-OCT).

Methodology/Principal Findings: Wild type (WT) and RP rabbits (aged 4–20 weeks) were investigated using SD-OCT. The total retinal thickness in RP rabbits decreased with age. The thickness of the outer nuclear layer (ONL) and between the external limiting membrane and Bruch's membrane (ELM–BM) were reduced in RP rabbits around the visual streak, compared to WT rabbits even at 4 weeks of age, and the differences increased with age. However, inner nuclear layer (INL) thickness in RP rabbits did not differ from that of WT during the observation period. The ganglion cell complex (GCC) thickness in RP rabbits increased near the optic nerve head but not around the visual streak in the later stages of the observation period. Hyper-reflective change was widely observed in the inner segments (IS) and outer segments (OS) of the photoreceptors in the OCT images of RP rabbits. Ultrastructural findings in RP retinas included the appearance of small rhodopsin-containing vesicles scattered in the extracellular space around the photoreceptors.

Conclusions/Significance: In the current study, SD-OCT provided the pattern of photoreceptor degeneration in RP rabbits and the longitudinal changes in each retinal layer through the evaluation of identical areas over time. The time-dependent changes in the retinal structure of RP rabbits showed regional and time-stage variations. *In vivo* imaging of RP rabbit retinas by using SD-OCT is a powerful method for characterizing disease dynamics and for assessing the therapeutic effects of experimental interventions.

Citation: Muraoka Y, Ikeda HO, Nakano N, Hangai M, Toda Y, et al. (2012) Real-Time Imaging of Rabbit Retina with Retinal Degeneration by Using Spectral-Domain Optical Coherence Tomography. PLoS ONE 7(4): e36135. doi:10.1371/journal.pone.0036135

Editor: Steven Barnes, Dalhousie University, Canada

Received November 27, 2011; **Accepted** March 26, 2012; **Published** April 27, 2012

Funding: This research was supported by Research grants from the Astellas Foundation for Research on Metabolic Disorders and the Japan Foundation for Applied Enzymology, and a Grant-in-Aid for Young Scientists (22791656) from the Ministry of Education, Culture, Sports, Science and Technology (MEXT). The funders had no role in study design, data collection and analysis, decision to publish, or preparation of the manuscript.

Competing Interests: The authors have declared that no competing interests exist.

* E-mail: hanakoi@kuhp.kyoto-u.ac.jp

Introduction

Retinitis pigmentosa (RP) is an inherited retinal disorder characterized by a progressive loss of visual function due to degeneration of rod and cone photoreceptors and eventual atrophy of the entire retina [1,2]. However, there are no effective treatments for RP. Various animal models of RP have been developed and studied to elucidate the pathophysiology of the disease and to develop new treatments [3–10]. Of these models, only monkeys have a macula, an important area for vision due to the high density of cone photoreceptors. However, it is not easy to study the pathophysiology of RP in monkeys due to handling and breeding difficulties. Rabbits are known to have a visual streak, where the rod and cone photoreceptor density is highest, about 3 mm ventral to the optic nerve head (ONH) [11,12]. Rabbits are easy to breed and handle, and the physiology and morphology of rabbit retina is well understood [11–14]. Additionally, in mid-sized animals like rabbits, surgical treatments such as subretinal injection of cells for regenerative therapy [15,16], vectors for gene therapy [17], and implantation of intraocular devices [18,19] are easily performed. Therefore, rabbits are very useful for studying retinal diseases and testing new therapeutic interventions. For these reasons, we used transgenic (Tg) rabbits with mutated rhodopsin (Pro 347 Leu, RP rabbits) as a mid-sized model for RP

[20] to study the pathophysiology and develop new evaluation systems for retinal degeneration.

Optical coherence tomography (OCT) devices allow non-invasive detection of retinal architecture, including quantitative measurements of retinal thickness and longitudinal observation of the retinal architecture [21]. The technological advances in spectral-domain OCT (SD-OCT) have enabled high-speed scanning and improved image resolution [22]. Furthermore, the exact averaging of B-scans with a three-dimensional eye-tracking system and high-speed scanning have enabled sufficient reduction in speckle noise, the most influential artificial noise that blurs the boundaries between retinal layers [23,24]. These advances have improved visualization of individual retinal layers, including both the outer retina and the inner retina (i.e., ganglion cell layer and inner plexiform layer [IPL] in humans) [25,26]. SD-OCT imaging also enables evaluation of the junction between the inner segment (IS) and the outer segment (OS) of the photoreceptors (IS/OS) [27–29] and that of the external limiting membrane (ELM) [30,31] as hallmarks of photoreceptor integrity. That is, visual function can be speculated from OCT images to some extent. Thus, the use of OCT imaging in humans has contributed to a more detailed understanding of the pathophysiology of many retinal diseases. In mice, the retina has been clearly visualized using SD-OCT [32–37]. Thus, in experimental animals, SD-OCT may allow *in vivo* detection and monitoring of changes in retinal architecture without sacrificing animals.

In mouse models of retinal degeneration, Fischer [36] and Huber et al. [32] detected and analyzed photoreceptor degeneration by using SD-OCT. They imaged the thinning of inner retinal layers and compared the total retinal thickness with that of normal mice in several mouse RP models. Yamauchi et al. reported the retinal architecture of rabbits by using SD-OCT following iodoacetic acid-induced photoreceptor degeneration [38]. However, retinal pathomorphology of genetically engineered rabbit models of RP, which mimic human RP [20], and longitudinal assessment of changes in the individual retinas remain to be studied with SD-OCT.

The purpose of this study was to visualize the time-dependent changes in photoreceptors, elucidate the pattern of changes in each retinal layer around the visual streak in identical eyes of RP rabbits by using SD-OCT, and assess the visual functions by electroretinography (ERG).

Results

Visualization of retinal structures in RP rabbits with SD-OCT

We first investigated whether the retinal structures of WT rabbits could be clearly visualized using SD-OCT. Vertical OCT images, which passed through the center of the ONH (Fig. 1A), permitted clear identification of each retinal layer, the choroid, and sclera of WT rabbits (Figs. 1B and 1C). The ELM and IS/OS lines were also clearly identifiable, the integrity of which have been shown to be positively associated with visual function. In the vertical OCT images, the scleral ring was defined as the edge of the ONH so that OCT measurements could be longitudinally compared between each rabbit and between WT and RP rabbits (Fig. 1B).

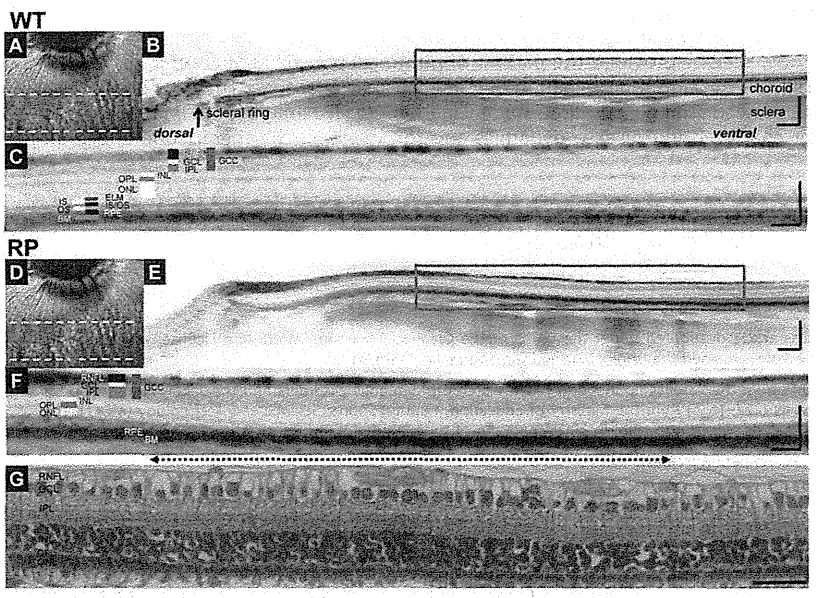

Figure 1. SD-OCT images of WT and Retinitis Pigmentosa (RP) rabbit retinas and histology of the visual streak in an RP rabbit. (A) A fundus infrared image of a WT rabbit retina, including optic nerve head (ONH) and visual streak. The area between dotted lines is the visual streak. (B) A vertical SD-OCT image along the green arrow in panel A, which passes through the center of the ONH. On this vertical image, the scleral ring was regarded as the lower margin of the ONH. (C) A magnified OCT image of the area enclosed by the blue square in panel B, which includes the visual streak. (D) A fundus infrared image of a RP rabbit retina, including the ONH and visual streak. (E) A vertical SD-OCT image of a 20-week-old RP rabbit along the green arrow in panel D. (F) A magnified OCT image of the area enclosed by the blue square in panel E. The 2.2 mm width of this OCT section was vertically cut between 1.8 mm and 4.0 mm ventral to the inferior edge of the ONH. A dotted arrow indicates the region of the visual streak. (G) Hematoxylin-Eosin staining of a retinal section corresponding to the area in the OCT image in F. Scale Bar = 200 μm (B, E), 100 μm (C, F), and 50 μm (G). RNFL, retinal nerve fiber layer; GCL, ganglion cell layer; IPL, inner plexiform layer; GCC, ganglion cell complex; INL, inner nuclear layer; OPL, outer plexiform layer; ONL, outer nuclear layer; ELM, external limiting membrane; IS, inner segments of photoreceptors; OS, outer segments of photoreceptors; IS/OS, junctions between IS and OS; RPE, retinal pigment epithelium; and BM, Bruch's membrane.
doi:10.1371/journal.pone.0036135.g001

Next, we examined a 20-week-old RP rabbit that expressed mutated rhodopsin (Figs. 1D–1F). The outer nuclear layer (ONL) of the RP rabbit was much thinner than the WT rabbit. Furthermore, in the RP rabbit, the photoreceptors around the visual streak (indicated by the dotted arrow), where the densities of rod and cone photoreceptors were the highest, appeared to be more severely damaged than in any other area. In this area, the ONL was very thin and the outer plexiform layer (OPL) was faint or absent depending on the distance from the ONH and the IS/OS line was undetectable (Fig. 1F). This regional variation in photoreceptor damage was also detected with hematoxylin and eosin (H&E) staining in the same eye (Fig. 1G).

Time-dependent changes in the photoreceptor layers and in the visual function of RP rabbits

As observations revealed that photoreceptor damage was severe around the visual streak, we were encouraged to investigate the time-dependent changes in the photoreceptors of identical RP rabbits beneath the visual streak with SD-OCT and compared them with those of the WT rabbits (Fig. 2A). At 4 weeks of age (with the youngest that can be examined by OCT), the ONL of RP rabbits was almost as thick as WT rabbits. Following 4 weeks of age, the ONL thickness in RP rabbits decreased. At 20 weeks, the ONL thickness in RP rabbits was much smaller than in WT rabbits. Photoreceptor IS and OS, where visual phototransduction occurs, were thin in RP rabbits. In contrast, the architecture of the inner retina was relatively preserved in RP rabbits at both 10 and 20 weeks of age.

In the current SD-OCT study, there were additional findings in the photoreceptor layers. In the sections of WT rabbits, the reflectivity of IS and OS was low compared to that of the ELM and IS/OS lines. In contrast, the IS and OS were highly reflective in RP rabbits, and almost equivalent to the ELM and IS/OS lines throughout the study ages (Fig. 2A).

To compare the SD-OCT data with those from the histological examination, histological sections of the age-matched RP and WT rabbits were prepared (Fig. 2B). The number of photoreceptors and thickness of the ONL, IS, and OS in the RP rabbits decreased with age, which is consistent with those of a previous report [20]. At 20 weeks of age, the nuclei of photoreceptors in RP rabbits were reduced to 1 or 2 rows, which was much less compared to WT rabbits. The magnitude of the decrease in ONL thickness appears similar between the histological and SD-OCT data (Figs. 2A and 2B). In the histological sections of a 4-week-old RP rabbit, the total retinal thickness and the ONL thickness were almost the same as those of the WT rabbit, and the IS and OS appeared intact. The high reflectivity in the IS and OS observed in the OCT sections was difficult to explain by the histological sections (Figs. 2A and 2B).

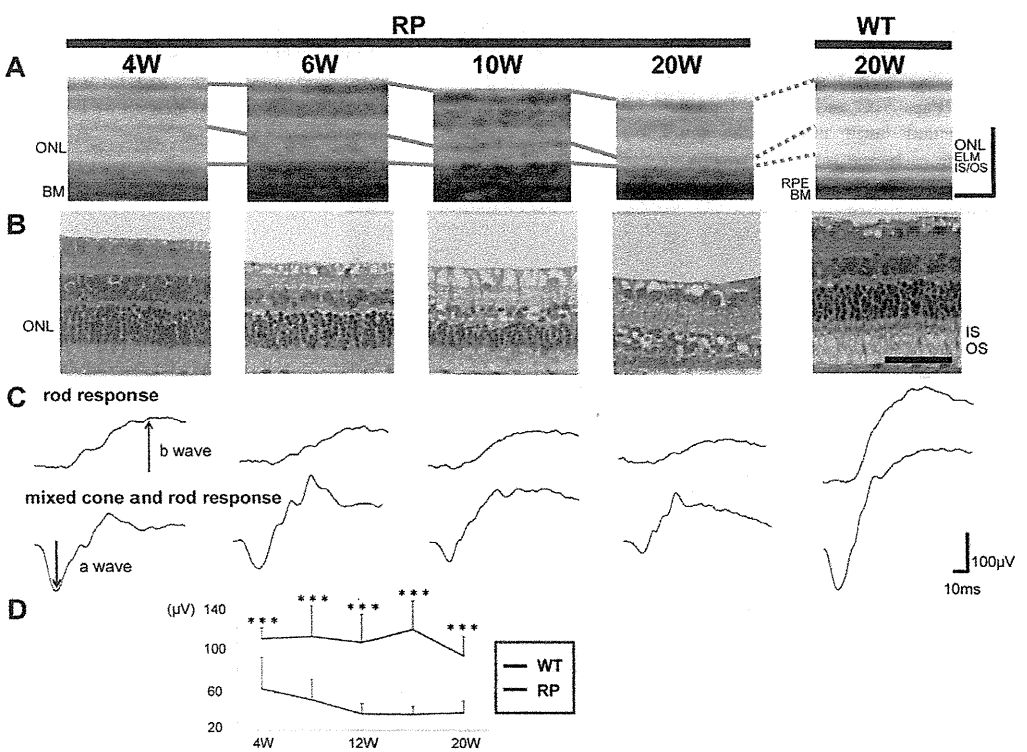

Figure 2. Time-dependent changes in morphological features of the retina and visual function in the RP rabbits. (A) SD-OCT images beneath the visual streak in an RP rabbit at 4, 6, 10, and 20 weeks and in a 20-week-old WT rabbit. The total retinal and ONL thickness in the RP rabbits decreased with age. The IS and OS were highly reflective in the RP rabbits compared with the WT rabbits. ONL, outer nuclear layer; and OS, outer segments of photoreceptors. (B) Hematoxylin-eosin staining of retinas in 4-, 6-, 10-, and 20-week-old RP and 20-week-old WT rabbits. The ONL in RP rabbits thinned with age. In 20-week-old RP rabbits, only 1–2 layers of nuclei were detected in the ONL. (C) Representative scotopic electroretinograms of 4-, 6-, 10-, and 20-week-old RP and 20-week-old WT rabbits. (D) The a-wave amplitude of the mixed rod and cone response. The amplitude was smaller in the RP rabbits than in the WT rabbits. The differences between the WT and RP rabbits were significant at all study points between 4 and 20 weeks. *$P<0.05$, ***$P<0.001$ (unpaired t-test). Scale Bar = 100 μm in A, and 50 μm in B. ONL, outer nuclear layer; ELM, external limiting membrane; IS/OS, junctions between inner segment (IS) and outer segment (OS); RPE, retinal pigment epithelium; and BM, Bruch's membrane.

doi:10.1371/journal.pone.0036135.g002

Next, to evaluate visual function of the rod and cone systems of RP rabbits, scotopic full-field ERG was recorded (Fig. 2C). The a-wave of the mixed cone and rod response, which mainly originates from the photoreceptors, was smaller in RP rabbits (61.2±30.5 μV) (mean ± SD) than in WT rabbits (110.3±10.7 μV; $P=0.010$, unpaired *t*-test) as early as 4 weeks. The a-wave amplitude was reduced with RP rabbit aged (Fig. 2D). At the age of 20 weeks, the a-wave amplitude decreased to 37.6±11.5 μV in RP rabbits and was significantly less than that of WT rabbits (93.5±19.0 μV; $P<0.001$, unpaired *t*-test, Figs. 2C and 2D). The b-wave amplitude of the rod response, which originates indirectly from bipolar and Müller cells, was 97.3±33.2 μV in RP rabbits and was less than that of WT rabbits (280.8±71.3 μV; $P<0.001$, unpaired *t*-test, Fig. 2C). These data suggest that the visual function of both the rod and cone systems was disturbed in RP rabbits, consistent with a previous report [20]. These results indicate that loss of photoreceptors and concomitant visual dysfunction gradually occurs in RP rabbits.

Vesicles cleaved from photoreceptors and disorganization of IS and OS in RP rabbits account for the hyper-reflectivity seen in SD-OCT images

To elucidate the cause of the hyper-reflective change in the outer photoreceptor layers of RP rabbits in SD-OCT sections, we examined and compared the ultrastructure of the retina between RP and WT rabbits at 4 or 20 weeks of age. In WT rabbits, the IS and OS exhibited a dense and regular arrangement (Figs. 3A, 3B, S1A and S1B). In contrast, in the RP retinas, the IS and OS were less organized at 4 weeks of age (Figs. 3C and 3D), and they were mostly absent at 20 weeks of age (Figs. S1C and S1D). Magnified images of the RP retinas revealed large number of small, approximately 100 nm, vesicles scattered in the extracellular space around the photoreceptors (arrowheads in Fig. 3D and S1D). These small vesicles appeared to be cleaved from the membrane of the IS in RP rabbits (arrows in Fig. 3E and S1D).The disrupted organization and the presence of vesicles between the IS and OS on ultra microscopy may account for the hyper-reflectivity seen in the corresponding area of the SD-OCT images.

To determine the origin of the vesicles, we performed ultrastructural immunohistochemistry by using monoclonal antibodies against rhodopsin (Fig. 3F). In RP retinas, numerous vesicles with dots were observed, indicating the presence of rhodopsin within the vesicles (disintermediated arrowheads in Fig. 3F).

Time-dependent changes in the individual retinal layers in SD-OCT sections exhibit regional and time-stage variations in RP rabbits

In the SD-OCT examinations, the retinal thickness in the RP rabbits appeared to decrease with age. Therefore, we quantitatively measured the mean total retinal thickness around the visual streak in the WT and RP rabbits (Figs. 4A and S2). As shown in Fig. 4A, the total retinal thickness in WT rabbits did not change with age, whereas that of the RP rabbits progressively decreased. The total retinal thickness in WT and RP rabbits was not significantly different at 4 weeks. However, after 6 weeks, the differences in the total retinal thickness increased and continued with age. At 20 weeks, the total retinal thickness in RP rabbits was 165.8±8.5 μm and significantly smaller than that of WT rabbits (194.3±7.7 μm; $P<0.001$, unpaired *t*-test).

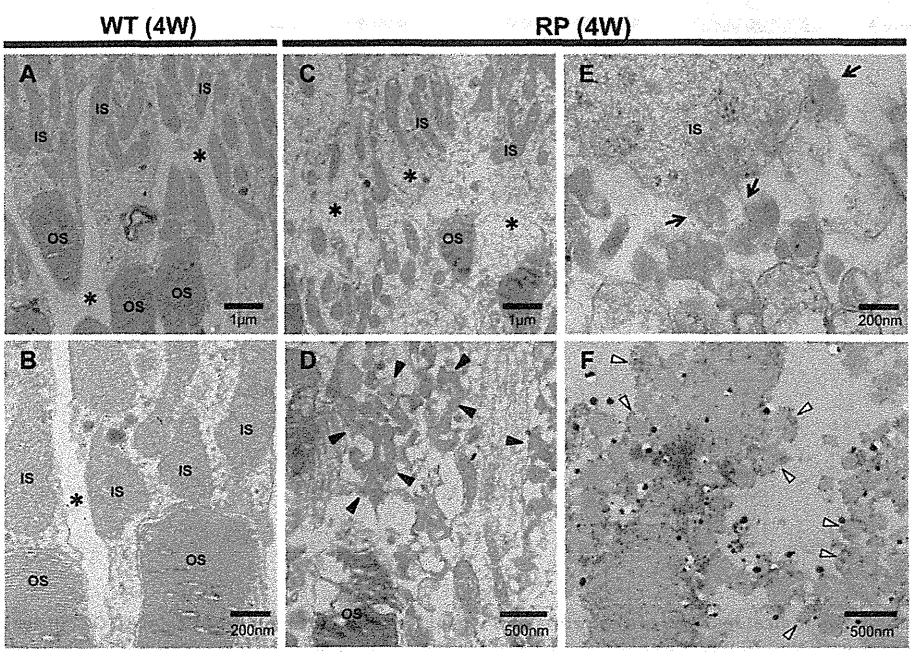

Figure 3. Ultrastructure of photoreceptors in WT and RP rabbits. (A, B) Ultrastructure of photoreceptors in 4-week-old WT rabbits. The inner (IS) and outer segments (OS) of the photoreceptors were regular and dense. There are no vesicles in the extracellular spaces (*). (C–E) Ultrastructure of the photoreceptors in the 4-week-old RP rabbits. The IS and OS were less organized than those in the WT rabbits. In the magnified image (D), the RP rabbit retina showing many small vesicles (arrowheads) accumulated in the extracellular spaces (indicated with * in panel C). The vesicles appeared to be cleaved from the IS into the extracellular space around the photoreceptors (arrows in panel E). (F) Ultrastructural immunohistochemistry by using an anti-rhodopsin antibody. The small vesicles (disintermediated arrowheads) in the extracellular spaces around the photoreceptors exhibit black dots indicating the presence of rhodopsin.
doi:10.1371/journal.pone.0036135.g003

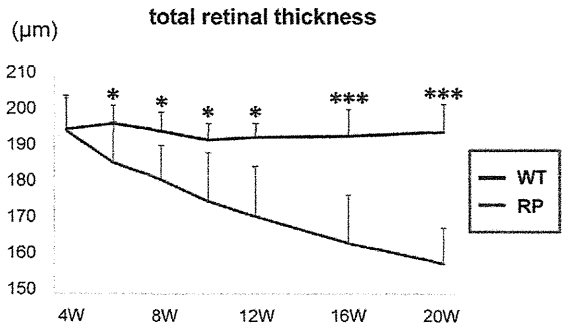

Figure 4. Time-dependent changes in total retinal thickness, and mixed cone and rod response in the WT and RP rabbits. The total retinal thicknesswas measured within a circle 1 mm in diameter 3 mm ventral to the lower margin of the ONH and averaged. The total retinal thickness in the WT rabbits (indicated with a blue line) was unchanged during observation, whereas that in the RP rabbits (indicated with a red line) severely decreased with age. *$P<0.05$, ***$P<0.001$ (unpaired t-test).
doi:10.1371/journal.pone.0036135.g004

OCT examination showed that the photoreceptors were most severely damaged at the visual streak, approximately 3 mm ventral to the ONH [11]. Therefore, we longitudinally examined regional and periodical variations in the progression of retinal degeneration in RP rabbits. For this purpose, we measured the thickness of each retinal layer within 0.5-mm areas 4 mm ventral to the lower edge of the ONH as a function of distance from the lower optic disc margin at 4, 6, 10, and 20 weeks by using the vertical OCT images that passed through the center of the ONH and visual streaks (Fig. S3).

ONL thickness. We first evaluated the thickness of the ONL where the nuclei of photoreceptors are located (Fig. 5A). In WT rabbits, the ONL in each area became slightly thinner with age. In younger WT rabbits (4–6 weeks old), the ONL was thinner in areas more distant from the ONH. In RP rabbits, the decrease in ONL thickness with age was more progressive than that of WT rabbits. At any age examined, thinning of the ONL was greater in areas more distant from the ONH. At 10 and 20 weeks, the ONL was thinnest in the area 3.0–3.5 mm ventral to the ONH.

At 4 weeks, the ONL thickness in RP rabbits was significantly less than that of WT rabbits in only the area 3.0–3.5 mm from the ONH ($P = 0.037$, unpaired t-test). Areas that exhibited a difference in ONL thickness between WT and RP rabbits expanded with age. At 20 weeks, the ONL thickness in RP rabbits was significantly smaller than that of WT rabbits in each of the 7 areas examined ($P<0.001$, unpaired t-test, Fig. 5E).

ELM–BM thickness. The ELM–BM thickness was evaluated because the area between the ELM and BM includes the length of the IS and OS where visual phototransduction occurs (Figs. 5B and S3). In WT rabbits, the ELM–BM thickness was larger in areas more distant from the ONH at any age examined. On the other hand, in RP rabbits, the differences in the ELM–BM thickness between areas as a function of distance from the ONH were smaller compared to those of WT rabbits at 4–10 weeks; the ELM–BM thickness appeared to decrease mainly in the areas distant from the optic disc. In 20-week-old RP rabbits, the ELM–BM thickness markedly decreased in the area 2.5–3.5 mm ventral to the ONH and was significantly less than that in the corresponding areas in WT rabbits ($P<0.001$, unpaired t-test, Fig. 5E).

INL thickness. The INL comprises the nuclei of bipolar, horizontal, amacrine, and Müller cells. The INL thickness was larger in areas more distant from the ONH in both WT and RP rabbits at the ages of 4 to 20 weeks (Fig. 5C). The INL thickness in WT and RP rabbits was not significantly different in each corresponding area at all the ages examined (Fig. 5E).

GCC thickness. The GCC consists of the retinal nerve fiber layer (axons of ganglion cells), ganglion cell layer (somas of ganglion cells), and IPL. To determine the influence of photoreceptor degeneration on the inner retina, GCC thickness was measured (Figs. S3 and 5D). The GCC thickness in the WT and RP rabbits exhibited a similar pattern in all the areas examined at the ages of 4 and 6 weeks. However, in 20-week-old RP rabbits, the GCC thickness in the areas close to the ONH was larger than in younger RP rabbits and in the corresponding areas of 20-week-old WT rabbits ($P<0.001$ for both, unpaired t-test, Fig. 5E).

In summary, the decrease in the ONL and ELM–BM thickness in RP rabbits was first detected in the areas approximately 3.0 mm ventral to the lower edge of the ONH (areas corresponding to the visual streak). Thinning of the IS and OS (measured as the ELM–BM thickness) followed thinning of the ONL. In contrast, the INL thickness in RP rabbits did not change throughout the observational period of 4 to 20 weeks. The GCC thickness in RP rabbits increased in areas away from the visual streaks but close to the ONH in the later phase of observation (Fig. 5E).

Discussion

In this study, we examined time-dependent changes in photoreceptor degeneration in identical RP rabbits, and compared the pattern of changes in individual retinal layers between WT and RP rabbits for the first time by using SD-OCT. In RP rabbits, we observed regional differences in the degree of photoreceptor loss. That is, the ONL (ONL: the somas of photoreceptors) in RP rabbits was thinnest beneath the visual streak, where the densities of rod and cone photoreceptors were the highest in WT rabbits, and the photoreceptors of RP rabbits were relatively preserved in the area near the ONH. The current observations by using SD-OCT revealed longitudinal changes in the RP rabbit retina that were fairly consistent with a previous histological study of the RP rabbits [20] and reports based on other animal models of RP [3,9].

To elucidate the unique "highly reflective IS and OS" feature of the outer photoreceptor layer during photoreceptor degeneration in RP rabbits, an electron microscopy study was conducted on 4- or 20-week-old RP rabbits. We detected vesicles around the photoreceptors and loss of most of the IS and OS. We speculate that these destructive structures in RP rabbits cause the hyper-reflectivity seen in the outer photoreceptor layers (between ELM and BM) on SD-OCT images (Fig. 2A).The vesicles appeared to be cleaved from the IS, as described in a previous report [20]. Moreover, these vesicles were shown to include rhodopsin by ultrastructural immunohistochemistry (Fig. 3F), indicating that the particles were derived from photoreceptors. In SD-OCT images of 4-week-old RP rabbits, the area between the ELM and BM was hyper-reflective even though the reflectivity and the thickness of the ONL were unchanged (Fig. 2A). These observations point to the mechanism by which photoreceptors degenerate in RP rabbits. That is, defective transport of rhodopsin from the IS to the OS, which was demonstrated in mice with mutated rhodopsin P347S by using an antibody against the mutated rhodopsin [39], is followed by cleavage of vesicles from the IS, and finally cell bodies of photoreceptors degenerate. It is speculated that early stage RP patients may have mutations in the rhodopsin gene if hyper-reflective patterns are detected with SD-OCT in the area corresponding to the IS and OS, though further studies are needed to confirm this speculation.

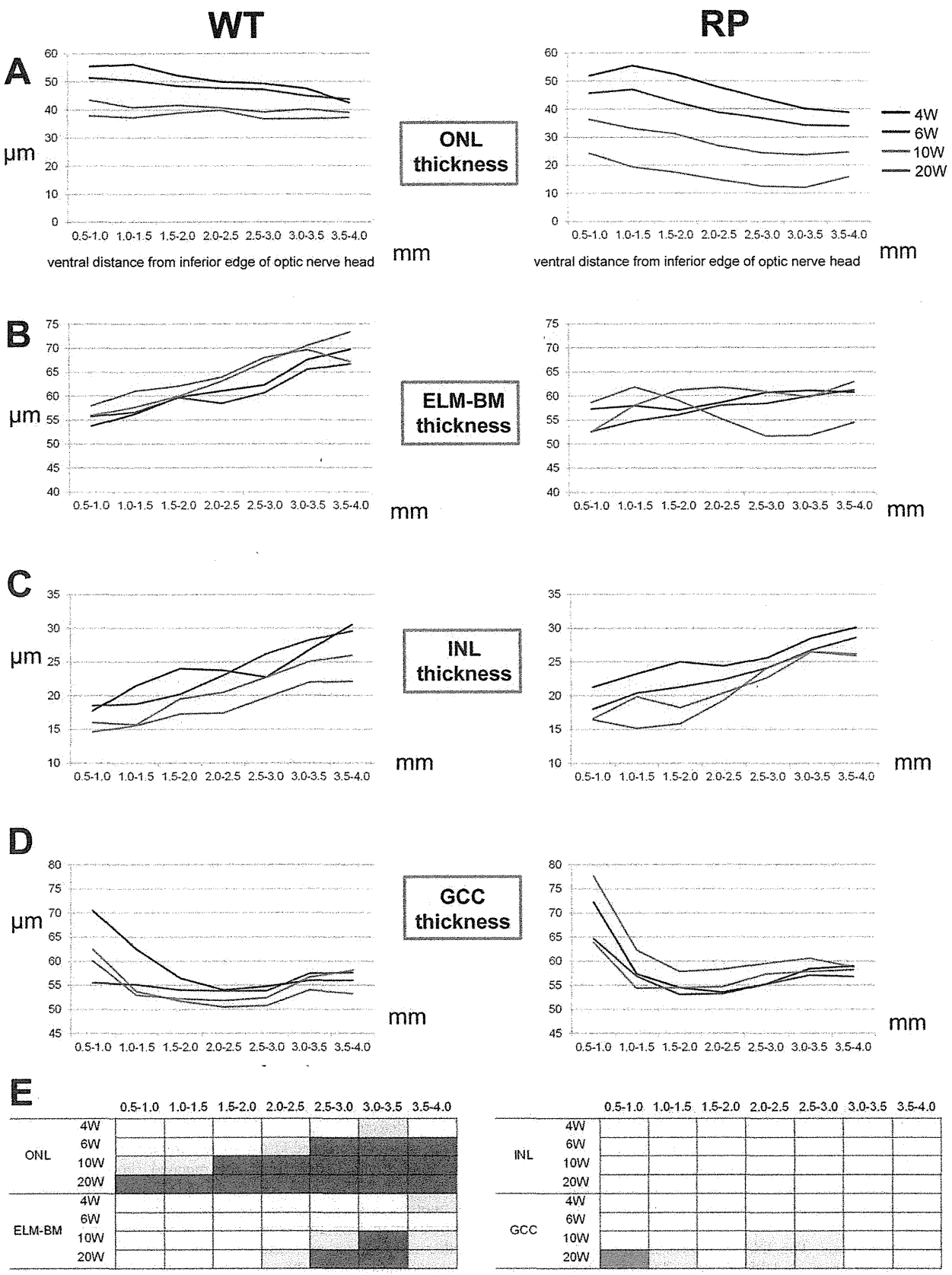
WT
RP
A
μm
ONL thickness
ventral distance from inferior edge of optic nerve head
mm
4W
6W
10W
20W
B
ELM-BM thickness
C
INL thickness
D
GCC thickness
E
ONL
ELM-BM
INL
GCC
0.5-1.0 1.0-1.5 1.5-2.0 2.0-2.5 2.5-3.0 3.0-3.5 3.5-4.0

Figure 5. Time-dependent changes in the thickness of individual retinal layers in WT and RP rabbits. (A–D) Time-dependent changes in ONL (A), ELM–BM (B), INL (C), and GCC (D) thickness measured with vertical OCT sections of WT and RP rabbits. Mean values at 4, 6, 10, and 20 weeks are indicated with blue, red, green, and purple lines, respectively. X-axes indicate the distance from the inferior edge of the ONH. (E) A schema to show time course and regional variations in the thickness of each retinal layer in RP rabbits from 4 to 20 weeks. Blue color indicates the regions where retinal thickness of RP rabbits was significantly smaller than that of WT rabbits. Orange color indicates the regions where retinal thickness of RP rabbits was significantly larger than that of WT rabbits. Deep and light colors indicate $P<0.001$ and $P<0.05$, respectively (unpaired *t*-test). ONL, outer nuclear layer; ELM, external limiting membrane; BM, Bruch's membrane; INL, inner nuclear layer; and GCC, ganglion cell complex.
doi:10.1371/journal.pone.0036135.g005

Aleman et al. reported the following disease sequence in human and murine RP caused by mutation of the rhodopsin gene: ONL diminution with INL thickening, amalgamation of residual ONL with the thickened INL, and progressive retinal remodeling with eventual thinning seen in OCT [40]. In our SD-OCT study, the INL thickness was not significantly different between WT and RP rabbits at the ages of 4 to 20 weeks. In contrast, the GCC thickness in RP rabbits paradoxically increased in the later phase of observation. Previous studies have suggested that the increase in the INL/inner retinal thickness in patients with RP maybe related to Müller glial activation with hypertrophy [40–42]. In the current study with RP rabbits, the observational period may be too short to detect an increase in INL thickness, or the gliosis of Müller cells may occur preferably within the GCC than in the INL.

This study has some limitations. The area imaged with SD-OCT was quite restricted such that the degeneration in RP retinas obtained with SD-OCT did not always correlate with the total retinal function. Furthermore, OCT or ERG could not be performed on rabbits younger than 4 weeks as their eyelids had not yet opened.

In conclusion, despite these short comings, *in vivo* time-dependent changes in the retinal structures were seen layer-by-layer in RP rabbits by using SD-OCT. These changes in the retinal structure had regional and temporal variations not only in the outer retina but also in the inner retina of RP rabbits. This study demonstrates that *in vivo* imaging with SD-OCT can facilitate the characterization of morphological disease dynamics and serve as a powerful tool for developing new treatments, such as gene therapy, intraocular devices, and neuroprotective treatments, in rabbit models of RP.

Methods

Experimental animals

This study was conducted in accordance with the Association Research in Vision and Ophthalmology (ARVO) Statement for the Use of Animals in Ophthalmic and Vision Research. All the protocols were approved by the Institutional Review Board of the Kyoto University Graduate School of Medicine (MedKyo11229).

New Zealand White rabbits (NZW, WT) and RP rabbits with rhodopsin P347L mutation (NZW, RP) [20] were purchased from Kitayama Labes Co., Ltd (Ina, Nagano, Japan). All rabbits were kept under a 14 h–10 h light-dark cycle (approximately 200 lux), given free access to water, and fed once a day. For the ERG recording and SD-OCT image acquisition, male WT (n = 4–10 eyes) and RP rabbits (n = 10–16 eyes) were used.

Retinal histology

Rabbit eyes were fixed overnight in a mixture of 10% neutral buffered formalin and 2.5% glutaraldehyde and then transferred to 10% neutral buffered formalin. The tissues were trimmed, embedded in paraffin, sectioned vertically through the optic nerve (superior-inferior), and stained with hematoxylin and eosin. The retina beneath the visual streak was examined and compared between 10- and 20-week-old WT and RP rabbits.

ERG

ERG was performed to assess the visual function of WT and RP rabbits at 4, 6, 10, and 20 weeks. Pupils were dilated with tropicamide (0.5%) and phenylephrine (0.5%) eye drops. Rabbits were dark-adapted for more than 60 min before anesthetization with an intramuscular injection of ketamine (25 mg/kg) and xylazine (2 mg/kg). ERG was recorded using a gold loop corneal electrode with a light-emitting diode (Mayo Corp., Inazawa, Japan). A reference electrode was placed in the mouth, and a ground electrode was attached to the ear. Stimuli were produced with a light-emitting diode stimulator (Mayo Corp.). The ERG response signals were amplified, digitized at 10 kHz with a band-pass filter of 0.3 to 500 Hz and analyzed (PowerLab 2/25; AD instruments, New South Wales, Australia). Two steps of stimulus intensities (ISCEV standard; scotopic 0.01 and scotopic 3.0) were used for evaluating rod and mixed cone and rod responses. The b-wave amplitude of the rod response and the a-wave amplitude of the mixed cone and rod response were analyzed.

SD-OCT

After ERG recording, rabbits were placed on a platform such that the visual streaks, which were approximately 3 mm ventral to the ONH, were located at the center of the image. The SD-OCT machine used in this study was *Multiline* OCT (Heidelberg Engineering, Heidelberg, Germany), which was customized based on a Spectralis HRA+OCT [37]. The *Multiline* OCT uses an 870-nm super-luminescent diode as a light source. The scan rate of the SD-OCT was 47,000 A-scans per second, with an axial resolution of ~7 μm.

Measurement and evaluations of total retinal thickness by using SD-OCT

To measure the total retinal thickness at the visual streak, a volume scan image was obtained (Fig. S2A). The lines of the vitreoretinal interface and BM were manually delineated at each horizontal section in a masked fashion (Figs. S2B and S2C). The mean total retinal thickness was measured within a red circle 1 mm in diameter, the center of which was 3 mm ventral to the inferior edge of the ONH, as determined by the software supplied by Heidelberg Engineering (Figs. S2D and S2E).

Measurements and evaluation of the thickness of retinal layers on vertical SD-OCT images

To measure and assess the thickness of each retinal layer, vertical OCT images, which passed through the center of the ONH and included the visual streak, were obtained by averaging 100 B-scans. To measure the thickness of the ONL, ELM–BM, INL, and GCC, the boundary lines between the OPL and ONL, ELM and BM, IPL and INL, and the vitreoretinal interface and IPL were manually delineated in a masked fashion (Fig. S3). The thickness of each retinal layer within the areas (0.5 mm each) 4 mm ventral to the lower edge of the ONH was measured as a function of distance from the lower optic disc margin by using the software supplied by Heidelberg Engineering (Fig. S3).

Electron Microscopy

The enucleated rabbit eyes were fixed in the same manner as the H&E stain. The eyes were subsequently fixed in 1% osmium tetroxide for 90 min. The retina was dehydrated through a graded series of ethanol (50–100%), cleared in propylene oxide, and embedded in epoxy resin. Ultrathin sections were cut by using an ultramicrotome and stained with uranyl acetate and lead citrate. For ultrastructural immunohistochemistry, the enucleated RP rabbit eyes were fixed in 4% paraformaldehyde and 0.05% glutaraldehyde for 4 h. The fixed retina was cut with a microslicer (Microslicer DTK-1000, Dosaka EM, Kyoto, Japan) into sections with a thickness of 65 μm. The sections were incubated with mouse monoclonal anti-rhodopsin antibody (Ret-P1 (sc-57433), Santa Cruz, California, U.S.A.) and subsequently, with gold-conjugated Fab fragment of goat anti-mouse IgG (Nanogold, Molecular Probes, Inc., Oregon, U.S.A.), followed by silver enhancement (HQ Silver, Nanoprobes, Inc., New York, U.S.A.). The stained sections were observed by transmission electron microscopy (H-7650, Hitachi Co., Tokyo, Japan).

Statistical analysis

Data from WT and RP rabbits were analyzed with an unpaired *t*-test by using PASW Statistics version 18.0 (SPSS Inc., Chicago, IL). The level of statistical significance was set at $P<0.05$.

Supporting Information

Figure S1 Ultrastructure of photoreceptors in 20-week-old WT and RP rabbits. (A, B) Ultrastructure of photoreceptors in 20-week-old WT rabbits. The inner segments of photoreceptors (IS) and the outer segments of photoreceptors (OS) were regular and dense. (C, D) Ultrastructural changes in 20-week-old RP rabbits. The IS and OS were mostly absent, and the residual IS and OS were less organized than those in WT rabbits. In the magnified image (D), many small vesicles (arrowheads) appeared to be cleaved from the IS into the extracellular space around the photoreceptors (arrows).
(TIF)

Figure S2 Measurement of mean total retinal thickness. (A) An infrared image on volume scan mode of SD-OCT. In the volume scan mode, the region ventral to the optic disc, including visual streak (19 lines in vertical 15° × horizontal 30°) was imaged. (B) One of the 19 horizontal OCT sections on volume scan mode. The lines of the vitreoretinal interface and the Bruch's membrane are manually delineated at each horizontal section (C). (D) The retinal thickness map constructed from the volume scan OCT images. Total retinal thickness was measured within the red circle shown (E). The diameter of the red circle was 1 mm, and the center was 3 mm ventral to the inferior edge of the ONH (D, E).
(TIF)

Figure S3 Measurement of the thickness of individual retinal layers. Four vertical OCT sections that pass through the center of the ONH and visual streak are shown. On each section, the boundary lines between each retinal layer were manually delineated. The ONL, ELM–BM, INL, and GCC thicknesses were evaluated in 0.5-mm segments as a function of the distance from the inferior optic disc margin up to 4.0 mm ventral to the inferior edge of the ONH. ONL, outer nuclear layer; ELM, external limiting membrane; BM, Bruch's membrane; INL, inner nuclear layer; and GCC, ganglion cell complex.
(TIF)

Acknowledgments

We thank MichikoTsuji, Yuri Terado, and Noriko Suzuki for their technical assistance; Megan Oliver for critical reading of the manuscript; Yuji Nishizawa of Chubu University for his advice on immunohistochemistry; and Gerhald Zinser of Heidelberg Engineering for discussion on the *Multiline* OCT. Presented in part at the Association Research in Vision and Ophthalmology (ARVO) Annual Meeting, May 2011; Florida, U.S.A.

Author Contributions

Conceived and designed the experiments: HOI YM NY. Performed the experiments: YM NN MH MK HT AK. Analyzed the data: YM. Contributed reagents/materials/analysis tools: YT KOF HK. Wrote the paper: YM HOI.

References

1. Hartong DT, Berson EL, Dryja TP (2006) Retinitis pigmentosa. Lancet 368: 1795–1809.
2. Mendes HF, van der Spuy J, Chapple JP, Cheetham ME (2005) Mechanisms of cell death in rhodopsin retinitis pigmentosa: implications for therapy. Trends Mol Med 11: 177–185.
3. Petters RM, Alexander CA, Wells KD, Collins EB, Sommer JR, et al. (1997) Genetically engineered large animal model for studying cone photoreceptor survival and degeneration in retinitis pigmentosa. Nat Biotechnol 15: 965–970.
4. Narfström K (1983) Hereditary progressive retinal atrophy in the Abyssinian cat. J Hered 74: 273–276.
5. Chader GJ (2002) Animal models in research on retinal degenerations: past progress and future hope. Vision Res 42: 393–399.
6. Petersen-Jones SM (1998) Animal models of human retinal dystrophies. Eye (Lond) 12(Pt 3b): 566–570.
7. Barnett KC, Curtis R (1985) Autosomal dominant progressive retinal atrophy in Abyssinian cats. J Hered 76: 168–170.
8. Menotti-Raymond M, David VA, Schäffer AA, Stephens R, Wells D, et al. (2007) Mutation in CEP290 discovered for cat model of human retinal degeneration. J Hered 98: 211–220.
9. Kijas JW, Cideciyan AV, Aleman TS, Pianta MJ, Pearce-Kelling SE, et al. (2002) Naturally occurring rhodopsin mutation in the dog causes retinal dysfunction and degeneration mimicking human dominant retinitis pigmentosa. Proc Natl Acad Sci U S A 99: 6328–6333.
10. Ng YF, Chan HH, Chu PH, To CH, Gilger BC, et al. (2008) Multifocal electroretinogram in rhodopsin P347L transgenic pigs. Invest Ophthalmol Vis Sci 49: 2208–2215.
11. Famiglietti EV, Sharpe SJ (1995) Regional topography of rod and immunocytochemically characterized "blue" and "green" cone photoreceptors in rabbit retina. Vis Neurosci 12: 1151–1175.
12. Rockhill RL, Daly FJ, MacNeil MA, Brown SP, Masland RH (2002) The diversity of ganglion cells in a mammalian retina. J Neurosci 22: 3831–3843.
13. Marc RE (1986) Neurochemical stratification in the inner plexiform layer of the vertebrate retina. Vision Res 26: 223–238.
14. Vaney DI, Young HM, Gynther IC (1991) The rod circuit in the rabbit retina. Vis Neurosci 7: 141–154.
15. Osakada F, Hirami Y, Takahashi M (2009) Stem cell biology and cell transplantation therapy in the retina. Biotechnol Genet Eng Rev 26: 297–334.
16. Stanzel BV, Liu Z, Brinken R, Braun N, Holz FG, et al. (2012) Subretinal delivery of ultrathin rigid-elastic cell carriers using a metallic shooter instrument and biodegradable hydrogel encapsulation. Invest Ophthalmol Vis Sci 53: 490–500.
17. Acland GM, Aguirre GD, Ray J, Zhang Q, Aleman TS, et al. (2001) Gene therapy restores vision in a canine model of childhood blindness. Nat Genet 28: 92–95.
18. Tao W, Wen R, Goddard MB, Sherman SD, O'Rourke PJ, et al. (2002) Encapsulated cell-based delivery of CNTF reduces photoreceptor degeneration in animal models of retinitis pigmentosa. Invest Ophthalmol Vis Sci 43: 3292–3298.
19. Bush RA, Lei B, Tao W, Raz D, Chan CC, et al. (2004) Encapsulated cell-based intraocular delivery of ciliary neurotrophic factor in normal rabbit: dose-dependent effects on ERG and retinal histology. Invest Ophthalmol Vis Sci 45: 2420–2430.
20. Kondo M, Sakai T, Komeima K, Kurimoto Y, Ueno S, et al. (2009) Generation of a transgenic rabbit model of retinal degeneration. Invest Ophthalmol Vis Sci 50: 1371–1377.
21. Wojtkowski M, Bajraszewski T, Gorczynska I, Targowski P, Kowalczyk A, et al. (2004) Ophthalmic imaging by spectral optical coherence tomography. Am J Ophthalmol 138: 412–419.
22. Chen TC, Cense B, Pierce MC, Nassif N, Park BH, et al. (2005) Spectral domain optical coherence tomography: ultra-high speed, ultra-high resolution ophthalmic imaging. Arch Ophthalmol 123: 1715–1720.
23. Sakamoto A, Hangai M, Yoshimura N (2008) Spectral-domain optical coherence tomography with multiple B-scan averaging for enhanced imaging of retinal diseases. Ophthalmology 115: 1071–1078.